UNIVERSIDADE ESTADUAL DE CAMPINAS

Instituto de Física “Gleb Wataghin”

Luiza Lober de Souza Piva

Condições iniciais utilizando PYTHIA para simulações hidrodinâmicas

Initial conditions using PYTHIA for hydrodynamic simulations

Campinas

2022

Luiza Lober de Souza Piva

Initial conditions using PYTHIA for hydrodynamic simulations

Condições iniciais utilizando PYTHIA para simulações hidrodinâmicas

Dissertação apresentada ao Instituto de Física
"Gleb Wataghin" da Universidade Estadual de Campinas
como parte dos requisitos exigidos para obtenção do
título de Mestra em física, na área de física.

Dissertation presented to the "Gleb Wataghin"
Institute of Physics of the University of Campinas
in partial fulfillment of the requeriments for the
degree of Master in Physics, in the area of Physics.

Supervisor: David Dobrigkeit Chinellato

ESTE TRABALHO CORRESPONDE À VERSÃO FINAL
DA DISSERTAÇÃO DEFENDIDA PELA ALUNA
LUIZA LOBER DE SOUZA PIVA, E ORIENTADA
PELO PROF. DR. DAVID DOBRIGKEIT CHINELLATO.

Campinas

2022

Ficha catalográfica
Universidade Estadual de Campinas
Biblioteca do Instituto de Física Gleb Wataghin
Lucimeire de Oliveira Silva da Rocha - CRB 8/9174

P688i

Piva, Luiza Lober de Souza, 1997-
Initial conditions using PYTHIA for hydrodynamic simulations / Luiza Lober de Souza Piva. – Campinas, SP : [s.n.], 2022.

Orientador: David Dobrigkeit Chinellato.
Dissertação (mestrado) – Universidade Estadual de Campinas, Instituto de Física Gleb Wataghin.

1. Fenomenologia de íons pesados. 2. Colisões entre íons pesados. 3. Simulação (Computadores). I. Chinellato, David Dobrigkeit, 1983-. II. Universidade Estadual de Campinas. Instituto de Física Gleb Wataghin. III. Título.

Informações para Biblioteca Digital

Título em outro idioma: Condições iniciais utilizando PYTHIA para simulações hidrodinâmicas
Palavras-chave em inglês:
Heavy ion phenomenology
Heavy ion collisions
Computer simulation
Área de concentração: Física
Titulação: Mestra em Física
Banca examinadora:
David Dobrigkeit Chinellato [Orientador]
Ernesto Kemp
Gabriel Silveira Denicol
Data de defesa: 18-04-2022
Programa de Pós-Graduação: Física

Identificação e informações acadêmicas do(a) aluno(a)
- ORCID do autor: https://orcid.org/0000-0003-1726-4152
- Currículo Lattes do autor: http://lattes.cnpq.br/8784246142979809

MEMBROS DA COMISSÃO JULGADORA DA DISSERTAÇÃO DE MESTRADO DA ALUNA LUIZA LOBER DE SOUZA PIVA - RA 173391 APRESENTADA E APROVADA AO INSTITUTO DE FÍSICA "GLEB WATAGHIN", DA UNIVERSIDADE ESTADUAL DE CAMPINAS, EM 18/04/2022.

COMISSÃO JULGADORA:

- Prof. Dr. David Dobrigkeit Chinellato - Presidente e Orientador (IFGW/UNICAMP)

- Prof. Dr. Ernesto Kemp (IFGW/UNICAMP)

- Dr. Gabriel Silveira Denicol (Instituto de Física - Universidade Federal Fluminense)

OBS.: Ata da defesa com as respectivas assinaturas dos membros encontra-se no SIGA/Sistema de Fluxo de Dissertação/Tese e na Secretaria do Programa da Unidade.

CAMPINAS

2022

"It's the questions we can't answer that teach us the most. They teach us how to think. If you give a man an answer, all he gains is a little fact. But give him a question and he'll look for his own answers."

Patrick Rothfuss, *The Wise Man's Fear*

Acknowledgements

I would like first to express my thanks to my advisor, Prof. Dr. David Dobrigkeit Chinellato, for his essential role in the development of this project and for all the discussions we've had throughout this work.

I'm thankful for all of the great feedback and conversations that I've had with the members of the HadrEx group, which allowed me to learn techniques and improve many aspects of my knowledge of particle physics and programming, being thus essential to this project. Special thanks goes to Willian Serenone and André Veiga Giannini for all the support and patience.

Also, I would like to thank all of the many friends I made and those that became even closer in these past two years, some of them having a direct or indirect contribution to this work, namely Ana Elisa Barioni, Matheus de Carvalho Loures, Luísa Pires Ferreira, Rafaela Ramos Sarmento, João Victor Ramalho Reis and Stefan Gerlach Braz Moreira.

I am also thankful to my parents, Luciane Lober de Souza, my mother, and Jayr Piva Júnior, my father, for always supporting my wish to become a physicist and making this journey possible.

I also would like to acknowledge the "Ministry of Science, Technology and Innovation" and the "National Council for Scientific and Technological Development – CNPq" for the grant 133488/2020-9 given to this project.

Resumo

Dentre as diversas questões em aberto da área de física de altas energias, a descrição teórica e a busca por sinais de um estado da matéria denominado plasma de quarks e glúons (QGP) são um grande desafio para sua teoria associada, a cromodinâmica quântica (QCD). Dada a complexidade considerável de procurar descrever a evolução de íons colisores altamente energéticos através de um conjunto fechado de equações, além de um volume abundante de dados experimentais para colisões na faixa de energias de TeV disponibilizado nos últimos anos, uma alternativa entre abordagens teóricas e previsões experimentais pode ser desenvolvida com o uso de modelos fenomenológicos, criados através de programas que simulam cada estágio de uma colisão de íons pesados

Neste trabalho, uma nova abordagem para simular as condições iniciais criadas nos momentos imediatamente posteriores de tais colisões foi desenvolvida através do uso de um pacote de códigos robusto conhecido como PYTHIA, que foi selecionado como o gerador de eventos para tal abordagem. As condições iniciais resultantes foram então caracterizadas e posteriormente evoluídas com o uso de uma cadeia hidrodinâmica de simulação, e os resultados finais obtidos destas simulações foram comparados com os dados experimentais disponibilizados pela colaboração ALICE.

Palavras-chave: Fenomenologia de íons pesados, Colisões entre íons pesados, Simulação.

Abstract

Within the list of open questions for the field of high-energy physics, the theoretical description and the experimental pursue of signals of a state of matter denominated quark-gluon plasma (QGP) provides a great challenge for its associated theory, quantum chromodynamics (QCD). Due to the considerable complexity of attempting to describe the evolution of highly energetic colliding ions with a complete set of equations, and given the abundant volume of data for experimental results in the range of TeV made available in recent years, a middle ground between a full theoretical approach and the experimental predictions can be reached with the use of phenomenological models, done through programs that simulates each step of a high-energy collision.

In this work, a new approach to simulate the initial densities created in the moments immediately after such collision was developed with the use of a robust code package known as PYTHIA as the event generator of choice. These resulting initial conditions were then characterized and later evolved through the use of a hydrodynamic simulation chain, with results being compared to experimental data provided by the ALICE collaboration.

Keywords: Heavy-ion phenomenology, Heavy-ion collisions, Simulation.

List of Figures

Contents

High energy physics and heavy-ion collisions

The extreme conditions of temperature and density resulting from ultrarrelativistic heavy-ion collisions in modern particle accelerators lead to the formation of strongly interacting matter, in which partonic degrees of freedom become relevant. This state of matter is known as Quark-Gluon Plasma (QGP), and the same conditions that gives rise to this plasma is believed to be the same present instants after the *Big Bang*. The full theoretical description of the states created in such collisions is an open challenge in the field of high energy nuclear physics. Observing, characterizing and studying its properties, with the objective of developing a better understanding of the fundamental interactions of matter, are the main motivations of this field of physics.

This first chapter is structured as a theoretical basis for the project. To this end, a general introduction to the field of particle physics, in the context of high energy collisions, will be presented. Sec. 1.1 will briefly introduce the main concepts of the Standard Model of particle physics, allowing then the discussion of the QGP formation phenomena and of its indirect measurements, which will be detailed throughout Secs. 1.1.1 and 1.1.2, respectively. The general properties of observables of heavy-ion collisions and relevant kinematic variables will also be presented in Sec. 1.2, along their experimental context.

1.1 The Standard Model

To understand the composition of known matter and its governing laws, one must first start with the study of the structure of the Standard Model of particle physics. This model is a remarkable feat of modern physics, characterized by its broad applicability in the fields of subatomic matter and its capability of providing very accurate results when compared to a myriad of experimental results, which ranges from several decades since the unification of the electro-weak force by Glashow, Weinberg and Salam [1–3]. Some of these experiments are currently performed within particle accelerators, with a

very prominent contribution being given by the experimental validation of the Higgs boson theory in the last decade, on the LHC accelerator [4–6]. High energy experiments can also be performed through observations of particle showers and decays, as done by the Pierre-Auger laboratory in its AugerPrime program [7], Auger Hybrid detector and many others.

The Standard Model is composed of elementary, or indivisible, particles and the three forces that are encased in the theory, with its equations dictating the dynamics of said components. Tab. 1.1 below lists the known elementary particles in order of discovery, where q stands for the electric charge of said particle, and numbers I to III represent the generation they belong to.

Table 1.1: Elementary particles of the Standard Model

Leptons				Quarks			
q	I	II	III	q	I	II	III
-1	electron (e^-)	muon (μ^-)	tau (τ^-)	$-1/3$	down (d)	strange (s)	bottom (b)
0	electronic neutrino (ν_e)	muonic neutrino (ν_μ)	tauonic neutrino (ν_τ)	2/3	up (u)	charm (c)	top (t)

It is important to note that, for simplicity, Tab. 1.1 does not enumerate the respective antiparticles, characterized by carrying negative charge $-q$, of each lepton and quark, and those particles can interact by the same means as the former ones through their respective mediator, as described in Tab. 1.2. Also, excluding neutrinos, which were not observed to go through decays − changing flavor as a consequence of an entirely different mechanism [8] − the more massive quarks and leptons of generation III are able to decay into the lighter generation II particles, and those, in turn, can decay into the lightest generation I quarks.

Of the total 64 particles included in the Model, the ones that can be directly observed are leptons and hadrons, with the latter being subdivided into baryons and mesons. Hadrons are formed from specific combinations of varying quarks and those, in turn, are characterized by a new quantum number known as “color”. Baryons are modernly defined as particles confining three RGB (red, green and blue) quarks, while mesons are generated with only two quarks of opposing color number. That definition comes from the principle of null color, in which the combination of quarks must be such that the sum of color in an observable particle is zero. This same color property is present in the mediators of the strong force known as “gluons”, composed of two color charges of opposing value.

It is important to note that, in phenomenological models, the term “parton”, specially in the context of Monte Carlo simulations in high-energy physics, is still very much used to refer to quarks

and gluons as an approximation, coming from the parton model first proposed by Richard Feynman. Partonic degrees of freedom will then refer to a state where the dynamics of quarks and gluons could be described considering a state of asymptotic freedom of those partons. This will be further discussed in Sec. 1.1.1.

The Standard model can be then summarized as shown in Tab. 1.2 below. In this work, the focus will be given to some implications of the strong interaction, governed by quantum chromodynamics. More specifically, the object of study is a state of matter known as quark-gluon plasma (QGP), which emerges given extreme conditions of temperature or pressure of a system of interacting particles, allowing for a deconfined state of quarks and gluons. The conditions in which such a plasma can be formed are described in the next section.

Table 1.2: Physical forces of the Standard Model, its mediators and the respective Quantum Field Theory (QFT) that describes their interaction. The "Particle" section refers to particles that can interact through said mediators

	Photon (γ)	W^+, W^-, Z^0	g (8 gluons)
Interaction	Electromagnetic	Electroweak	Strong
Theory	Quantum Electrodynamics	Electroweak Theory	Quantum Chromodynamics
Charges	Electric	Electric and Weak	Color
Particles	Charged Leptons Hadrons and Quarks	Leptons, Hadrons and Quarks	Quarks and Gluons

1.1.1 Asymptotic freedom

First, it is important to understand how the coupling of quarks and gluons take place in the QCD theory. This effect is observed quantitatively in the dependency of the coupling constant of the strong interaction α_s with the center of mass energy of the system, given by

$$\alpha_s \approx \frac{2\pi}{\beta_0} \frac{1}{\ln(Q^2/\Lambda_{\mathrm{QCD}})} \tag{1.1}$$

where Q^2 is the square of the total energy of the system, Λ_{QCD} is a scale parameter, with $\Lambda_{QCD} \approx 220$ MeV for hard interactions − defined by high momentum exchanges and a characteristic of high energy collisions. Also, β_0 is a constant, first shown to be negative for quantum chromodynamics by Wilczek,

Gross and Politzer [9]. This latter property is what enables the coupling constant to decrease at high energies, as shown below in Fig. 1.1 for increasing Q.

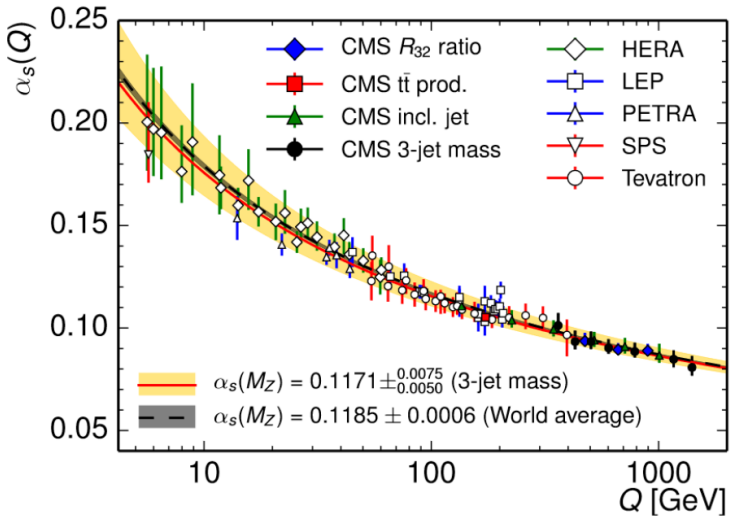

Figure 1.1: Different measurements of the coupling constant α_s as a function of Q, where the black curve indicates the theoretical predictions, obtained using lattice QCD calculations. Adapted from [10].

An important remark is that, when in this regime of weak coupling, perturbative quantum chromodynamics (p-QCD) can be used to analyse such systems of quarks and gluons instants after the collision takes place, in which its cross sections can be calculated with reasonable precision. However, with increasing values of α_s, the results for strongly-coupled quark-gluon plasma (s-QGP) must be obtained through non-perturbative methods, such as lattice QCD calculations [11, 12].

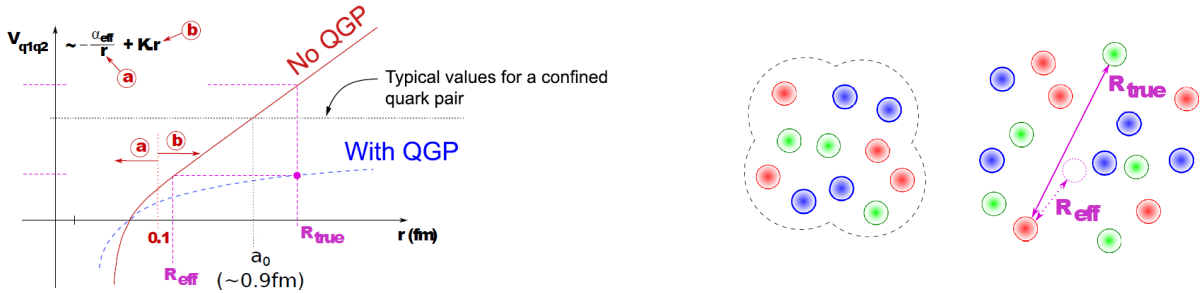

Figure 1.2: (a) Schematic representation of the effective interaction potential between a quark-antiquark pair, with a illustration of high-density states and the deconfinement of partons on (b). Figures from [13].

To understand the phenomenon of asymptotic freedom, the equation describing the effective potential of quark-gluon interaction will also be studied. It can be shown [10] that this potential assumes the following form

$$V_{eff} = -\frac{4}{3}\frac{\alpha_s(r)\hbar c}{r} + kr. \tag{1.2}$$

Notice that, for small distances r, that is, $r \leq 0.1$ fm, V_{eff} has the same behavior of a Coulomb potential and, for larger distances ($r \geq 1.0$ fm), this effective potential could be compared to the elastic interaction of classic mechanics, allowing it to be interpreted as a string tension between the quark pair.

In this first regime, the small distances between quarks, where the r is low enough to be in the range of effects of the strong force, are a result of the extreme conditions of pressure or temperature that the system is subjected to. The result of lattice QCD calculations in this condition predicts an increase in the degrees of freedom of the system composed of quarks and gluons. This points to a reduction of the effective potential of Eq. 1.2, allowing an state of asymptotic freedom for those particles, which characterizes the quark-gluon plasma. This is also reflected in the values of the coupling constant at those regimes, of around $\alpha_s \approx 0.1$ as shown before in Fig. 1.1, a condition that allows quarks to be treated as quasi-free particles inside this volume of high energy density, which is predicted by lattice QCD to be around $\varepsilon_c \approx 1\text{GeV fm}^{-3}$, or approximately 170 MeV.

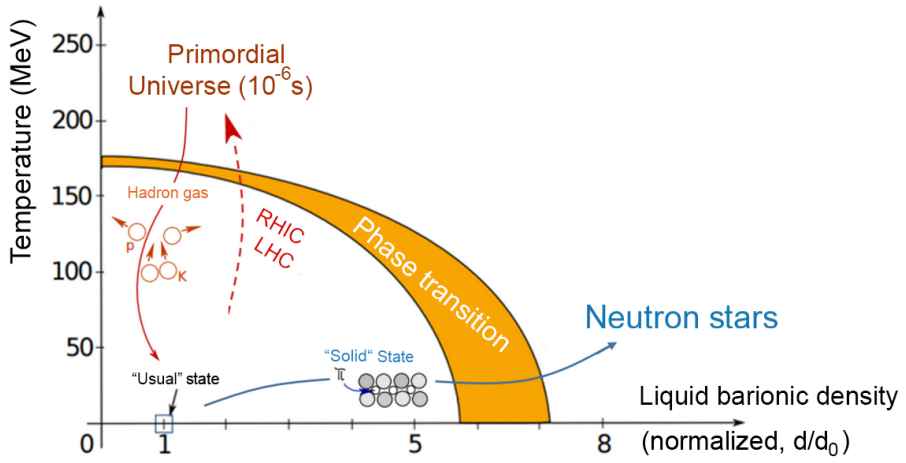

Figure 1.3: Schematic representation of the phase transition predicted by lattice QCD calculations in different regimes of temperature and barionic density. Adapted from [13].

For ultra-relativistic heavy-ion collisions, the temperature of the system of colliding particles will surpass this estimate temperature, which is predicted to be enough for the phase transition of ordinary matter to QGP to occur [12]. In this regime, it would then be possible to observe evidence of the existence of this state of matter. The discussion of such a phase transition has been very active in the past few years, and for a review on the topic in the context of RHIC's experiments with beam energy

scan, see [14].

The resulting observables from those experiments would then be correlated to the QGP formation through the measurement of signals associated with the plasma evolution, and detecting these signals is one of the main objectives of the ALICE collaboration at CERN, which was also essential to this project for providing the experimental data that was used throughout this work. More on the indirect evidence of existence of the QGP follows in the next section.

1.1.2 Possible QGP signals

The predicted QGP stage is very short lived, with its expected duration being in the order of 10 fm/c [15], or around 10^{-23} seconds. For this reason, it is impossible to measure the plasma directly, and indirect measurements, given by a combination of observables expected from the QGP formation on ion-ion (AA) collisions, is the current way of probing the presence of such state of matter. These results vary with the configuration of the initial states of the collision, and the effects of the emergence of QGP need also to be different from the those already known to be part of proton-proton (pp) collisions. Some of them are:

1. **Non-zero elliptic flow**: A very distinct characteristic of ion-ion collisions, when first compared to pp experiments, is the existence of a collective behavior observed in the propagation of produced particles. This anisotropic propagation is caused by the evolution of the fluid formed by the deconfined quarks and gluons after the collision process. This discovery was made through the observation of a large azimuthal anisotropy, or modulation of the propagation of those emitted particles, and known as elliptic flow (v_2), where non zero results were first observed at RHIC [16] for AA experiments. This observation is consistent with the predictions of nearly ideal hydrodynamics of the s-QGP discussed previously, thus endorsing the need of non-perturbative QCD in the modeling of this fluid. Note that such collective behavior is what allows for a hydrodynamic approach to be valid for the QGP;

    - Recent observations of relativistic collisions on smaller systems (pp, pA, $d+Au$ and ${}^3He+Au$) shows that those can also present anisotropy on the azimuth for its resulting particles, as discussed in [17].

2. **Particle production ratios**: when comparing pp and AA results, it is clear that there is a divergence in the ratio of multiplicities of observed particles in both experiments. Among

other reasons, this effect can be caused by the difference in the distribution of momentum of the participating partons in each case. This measurement could also be sensitive to phase transitions, such as the one predicted for the QGP [18];

3. **Transverse momentum spectra**: this quantity can be measured either considering each individual species of particles, such as $\pi, p, \bar{p}$ and, Ω, to observe jet production and correlations for high momenta; or through the mean distribution of transverse momenta, $\langle p_T \rangle$. This latter approach also correlates with the multiplicity of particles, and is a way to quantify the split of the energy of the system between particle production and kinematic energy of each particle.

There are several other possible ways of investigating QGP formation, such as strangeness production [19], jet fragmentation [20], heavy quark production [21], and many others [11]. This project will be focused in presenting results in Sec. 5 of multiplicity distributions and the anisotropy of simulated lead-lead (or Pb+Pb) heavy-ion collisions, in which the acquired outputs of the simulation will be compared to experimental observables.

1.2 Heavy-ion collisions

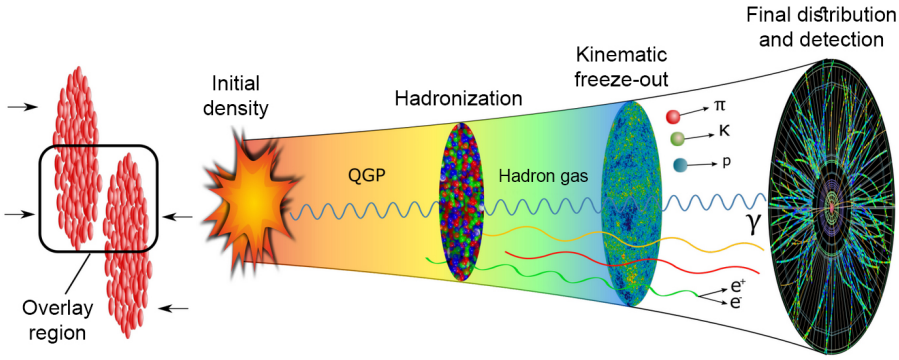

Figure 1.4: Representation of each heavy-ion collision stage, with the evolution occurring from left to right. Figure from [22].

To help visualize the process of colliding heavy-ions, Fig. 1.4 illustrates the main stages of such collision. From left to right, they are:

1. **Initial hard scattering**, where the first interactions between participant nucleons occur, being characterized by high-momentum-transfer processes. The reaction will take place in the region overlay region of the two nucleus;

2. **Thermalization** of the initial energy density of partons generated instants after the collision, with an intense production of particles and the expansion of the system. This energy density would be high enough to allow the phase transition of the system into the QGP;

3. **Hadronization**, where the distribution created by the initial density begins to cool down, with quarks and gluons combining into hadronic matter;

4. **Chemical *Freeze-out***, characterized by the end of inelastic interactions and the stabilization of the chemical composition of the system;

5. **Kinematic *Freeze-out***, ceasing all kinematic interactions between hadrons. The experimental measurements occurs shortly after.

Those stages will also be discussed in the following chapters. The entirety of Chap. 2 is dedicated to the study of initial conditions, while Secs. 3.1 and 3.2 of Chap. 3 will lay out the theoretical basis for the hydrodynamic procedure, which is presented along with computational considerations.

1.2.1 Kinematic properties

The energy of the collision

In a collision between two nucleons, say A and B, where A is the projectile and B the target at rest in the lab frame, Eq. 1.3 correlates the energy given in this frame and in the center of mass:

$$E_{cm} = \sqrt{(2E_{lab} + m_B)m_B + m_A^2} \tag{1.3}$$

where E_{cm} is the energy in the center of mass frame, E_{lab} the equivalent energy in the lab frame and $m_{A,B}$ are the masses of each colliding nucleon, with $c = 1$ also being used for the following calculations.

For a generic collision, one can define the quantity s as

$$s = \left(\sum_{i=1}^{2} E_i\right)^2 - \left(\sum_{i=1}^{2} \mathbf{p_i}\right)^2 . \tag{1.4}$$

E_i and p_i represents, respectively, the total energy and momentum of each colliding particle. This, along with u and p constitutes the set of Mandelstam variables [23], which are invariant under Lorentz transformations and comprises information of the energy and momentum of particles in scattering processes.

Note that, for the relativistic limit, the momenta of the particles will essentially constitute the total energy of the system E, thus allowing the approximation $E^2 = \mathbf{p} \cdot \mathbf{p} + m_0^2 \approx \mathbf{p} \cdot \mathbf{p}$, resulting in $s = E_{cm}^2$. The square root of this quantity is the usual variable used to quantify the system's energy in heavy-ion collision experiments and, for all results that will follow in Sec. 5, the energy will also be presented in this way, such as the chosen center-of-mass energy of $\sqrt{s} = 2.76$ TeV used throughout the simulations.

The collision's geometry

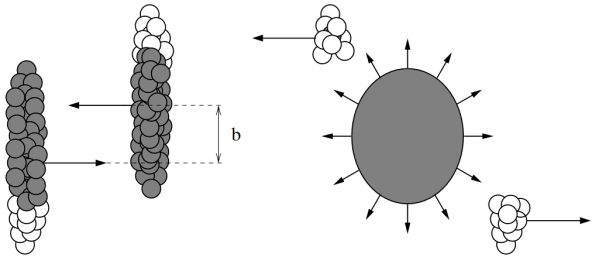

Figure 1.5: The initial stages of a heavy-ion collision. Left: instants before the collision takes place, with the participant nucleons drawn in dark grey and the impact parameter b defining the interacting area. Right: initial density created from the collision of the participants. Figure from [24].

One of the many ways to quantify how head-on or peripheral a collision will be is done by using the transverse distance between each nucleon center as a parameter. This variable is known as impact parameter (b), and can be used to estimate the centrality of a collision through the following relation:

$$c(b) = \frac{\int_0^b \frac{d\sigma}{db'} db'}{\int_0^\infty \frac{d\sigma}{db'} db'}, \tag{1.5}$$

where σ is the cross section of the collision. This variable then defines, from zero to one, the fraction of nucleons that will be included in the collision, or participant nucleons: the closer to one, the more central will the event be. In experimental results, the centrality of a collision is commonly presented as a percentual interval, such as $40 - 50\%$.

It is important to note that obtaining the impact parameter b of each nucleon, and as a consequence, the centrality in terms of b, is not experimentally possible, given that the length of each of those colliding ions is of the order of femtometers (10^{-15} m). This parameter is only accessible in simulations, and as such more accessible variables must be used in its place, as discussed in the following section.

1.2.2 Quantifying observables

Determining centrality

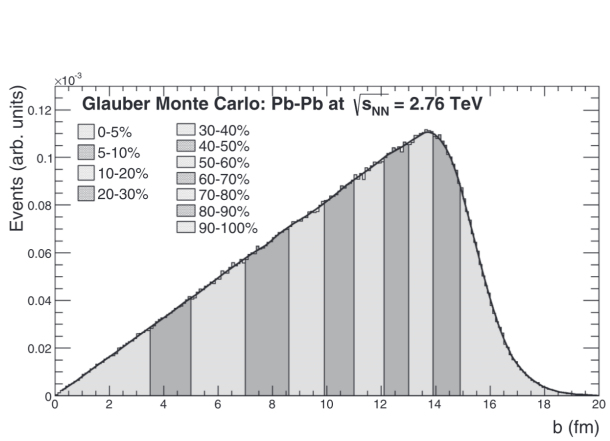

(a)

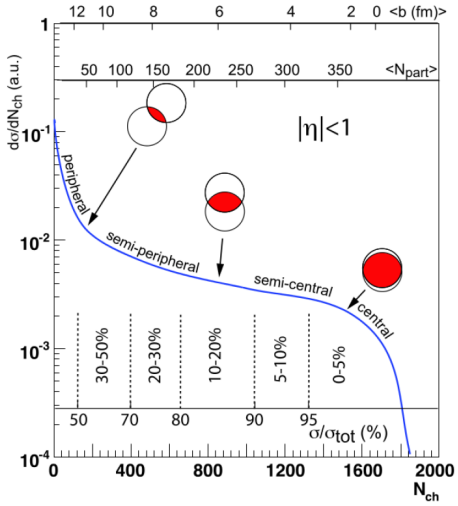

(b)

Figure 1.6: (a) Distribution of events by centrality and its relation to the impact parameter. The data is adjusted using a Monte Carlo fit as described in Sec. 4.1. Figure from [25]. (b) Dependency of the number of charged particles with the collision parameters b, σ and number of participants, illustrating the use of multiplicity as a way to determine centrality classes in experiments. Figure from [26].

From Fig. 1.6, it can be seen that the multiplicity of events is directly correlated to the impact parameter, with the division of those classes indicated in Fig 1.6a being a possible type of calibration of centrality for a given event.

Kinematic variables

The following parameters are also useful to characterize byproducts of heavy-ion collisions. First, the rapidity y of a particle, which is a ratio of a particle's forward to backward light-cone momentum, will be defined:

$$y = \frac{1}{2} \ln \left(\frac{E + p_z}{E - p_z} \right), \tag{1.6}$$

with E and p_z being the components of the four-momenta of such particle, given by

$$p^\mu = \left(p^0, p^1, p^2, p^3\right) = (E, \mathbf{p}) = (E, p_x, p_y, p_z), \tag{1.7}$$

with $c = 1$.

In classical mechanics, $y = v$, where v is the velocity of the particle in the longitudinal direction. However, the collisions that will be analysed all happen in the relativistic picture. In this context, the *pseudorapidity* of a particle can be defined and compared to rapidity,

$$\eta = -\ln\left[\tan\left(\frac{\theta}{2}\right)\right] = \frac{1}{2}\ln\left(\frac{|\mathbf{p}| + p_z}{|\mathbf{p}| - p_z}\right). \tag{1.8}$$

Note that, considering ultrarrelativistic collisions, the approximation $p_z \approx E\cos\theta$ is used to arrive at this result, and $p_T = \sqrt{\mathbf{p}^2 - p_z^2}$ is the transverse momentum of a particle.

The pseudorapidity has advantages over rapidity: in detector-based experiments, only the angle of the detected particle relative to the beam axis is available, and Eq. 1.8 shows that such measurement would be enough to determine pseudorapidity, as this is a geometrical variable. Also, it can be measured in the lab or center of mass frame. The relation between rapidity and pseudorapidity, given by [11], in terms of this second variable, will be

$$y = \frac{1}{2}\ln\left(\frac{\sqrt{p_T^2\cosh^2(\eta) + m^2} + p_T\sinh(\eta)}{\sqrt{p_T^2\cosh^2(\eta) + m^2} - p_T\sinh(\eta)}\right). \tag{1.9}$$

An important characteristic of such variables is that the peak values of multiplicity distribution in the center of mass frame is around $y \approx \eta \approx 0$ - in which other variables such as the energy of the system are normally measured, as discussed in Sec. 1.2.1 and shown in [11]. In this project, in order to match the experimental results studied, the range in pseudorapidity is taken to be $|\eta| < 0.8$.

Initial conditions

The initial stages of a heavy-ion collision is given by the instants shortly before and after the collision takes place. As the nucleons interact, an energy density profile will be generated, which are known to hydrodynamics simply as their initial conditions, modeling the geometric and kinematic properties of such initial stages. A full description of how the colliding nucleus will be located in space and how the posterior energy density is formed allows for the calculation of its evolution through fluid-like dynamics, being thus an essential step for the implementation of any hydrodynamic simulation.

In this chapter, the main properties of the initial stages, such as their geometry, will be discussed in Sec. 2.1. Sec. 2.2, will then present already well-known approaches to modeling this stage, with Sec. 2.3 being entirely dedicated to the PYTHIA event generator: a code capable of bringing rich physics to the early stage modelling of a collision. Finally, Sec. 2.4 will discuss the methodology developed in this project to adapt the outputs given by PYTHIA into an energy-momentum tensor for hydrodynamics.

2.1 Geometric properties of initial distributions

One way of quantifying the shape of the initial condition is to define its distribution with respect to a given geometry. Eccentricity, a two-dimensional measure of the correlation of a certain density to a circular geometry, can be mathematically defined as follows [27, 28],

$$\epsilon_2 = \frac{\sqrt{(\sigma_y^2 - \sigma_x^2)^2 + 4(\sigma_{xy})^2}}{\sigma_y^2 + \sigma_x^2}, \tag{2.1}$$

where σ_x^2, σ_y^2 and $\sigma_{x,y}^2$ are the covariances of the participant nucleon distributions in each direction. Shifting the reference frame to match the center of mass frame of the collision and generalizing for the desired geometry, this definition becomes

$$\epsilon_n = \frac{\sqrt{\langle r^2 \cos(n\phi_{part})\rangle^2 + \langle r^2 \sin(n\phi_{part})\rangle^2}}{\langle r^n \rangle}, \tag{2.2}$$

where r and ϕ_{part} are the polar coordinates of the participant nucleons.

In Eq. 2.2, each value of n correspond to a specific geometry: $n = 2$ specifies the eccentricity of the collision, $n = 3$ the triangularity, $n = 4$ the quadrangularity and so on, measuring then the contribution, or how similar the nucleon distribution will be to those shapes.

One could also correlate the initial condition geometry with the anisotropy produced in heavy-ion collisions, as shown in [29, 30]. This connection will be done in Sec. 4.2.1, after the concept of anisotropic flow is defined quantitatively.

2.2 Commonly employed approaches

There are many approaches for the modelling of initial conditions for hydrodynamics already being used in phenomenological models. Some of them are the IP-Glasma [31] formulation, the NeXuS package [32] and the Glauber-Montecarlo TRENTo code [33, 34]. Here, given that the results presented in Chap. 5 also included TRENTo's initial conditions as a baseline for developing the methodology on 2.4, this model will be described in greater detail in the next section.

2.2.1 The TRENTo parametric model

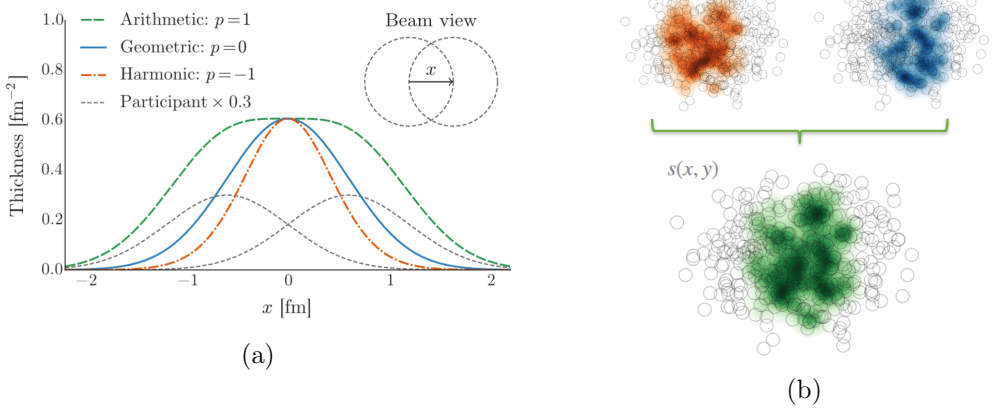

(a) (b)

Figure 2.1: (a) Behavior of the reduced thickness function for each value of p chosen. (b) Resulting entropy distribution $s(x, y)$ from the collision of nucleus A and B. Figures from [33]

The modeling of TRENTo is based on a Monte Carlo algorithm to generate the initial density profiles, describing the multiplicity distributions of nucleon-nucleon collisions of interest and staying consistent with experimental bounds. Its defining characteristic is to present those results without assuming entropy production, thermalization or pre-equilibrium dynamics mechanisms. Also, each nucleus is treated as a collection of nucleons, which allows the entropy distribution to be understood as a superposition of pp collisions.

For its computational implementation, the positions of colliding nucleus A and B are sampled via a Woods-Saxon equation that does not assume any correlation between them. With that, the probability of collision is calculated and only the colliding nucleons are saved for latter stages. The resulting thickness function of each nucleus given by

$$T_{A,B} = \sum_{i=1}^{N_{part}} w_i \int dz \rho_{proton}(x - x_i, y - y_i, z - z_i), \tag{2.3}$$

where w_i are random weights sampled from a gamma distribution $\Gamma(\mathbf{x})$ to introduce additional multiplicity fluctuations and fit experimental results, and ρ_{proton} is the matter density of each nucleus, generally modeled by a gaussian function.

The total energy distribution of the system can then be calculated using the *reduced* thickness formulation,

$$s(x, y) \propto \left(\frac{T_A^p + T_B^p}{2} \right)^{1/p}, \tag{2.4}$$

where p is a parameter determined experimentally.

This result is then used to fill the energy density entry of the energy-momentum tensor and allow for the simulation of the hydrodynamic behavior of the plasma. Note that, as mentioned before for this model, there's no clear physical mechanism included into the code, with these being only parametric solutions to energy densities generated by heavy-ion collisions, thus making very few assumptions of the collision process.

2.3 The PYTHIA event generator

In the same way as TRENTo, PYTHIA also uses a Monte Carlo algorithm for its sampling of nucleons. However, it goes beyond a parametric approach by including several formulations derived from QCD theory, and specially p-QCD. This is one of the most complete generators for pp collisions − and recently also capable of doing pA and AA events, as discussed in Sec. 2.3.3 − in terms of the amount of physical processes that can be applied to a collision event, and is being constantly updated to include recent experimental results into its phenomenological parameters.

For this project, a modified version of PYTHIA 8.235 was used. A full description of the physics included in the original release is done on [35], while most of its computational implementations being found on [36].

2.3.1 Interactions simulated in PYTHIA

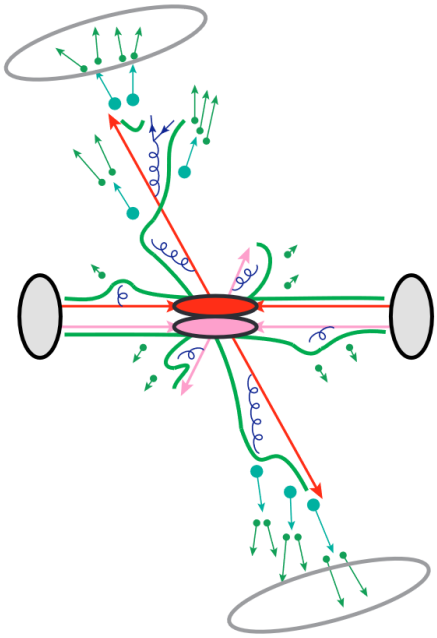

Figure 2.2: An schematic representation of the physical processes taking place during an event generation in PYTHIA. The colors represent: hard interactions (red), radiative cascade of partons (blue), interaction of initiators (pink), hadron formation (light green) and decays (dark green), and beam spectrum (grey). Figure from [37].

PYTHIA is able to simulate decays of particles, interactions between multiple partons and the hadronization process of quarks and gluons, to mention a few of its capabilities. Those effects are of great relevance to the physical aspect of early stage modelling, and PYTHIA is unique in allowing an approach for some of these phenomena. Below, some of the processes listed in Fig. 2.2 will be discussed.

Hard processes: Hard scatterings, as discussed before in Sec. 1.2, are characterized by their high-momentum transfer, in the scale of Q^2, along with large values of transverse momentum (p_T) or mass (m) of partons. In PYTHIA, they are processes of interaction between quarks (q) and gluos (g), or $qg \to qg$ processes.

Soft processes: These processes does not involve high transfers of momenta between particles, and some examples are the diffractive and elastic scatterings that can occur in partonic interactions. Notice that those processes are done using lattice QCD models, as the coupling between partons is stronger. The special treatment for those scatterings are discussed in Secs. 11.2-11.4 of [35].

Hadronization: This stage initiates at a given temperature that estimates the start of local

equilibrium, which in turn allows for partons to combine into hadronic matter without assuming the production of a fluid such as the QGP. PYTHIA is able to simulate the hadronization process, generating the species expected from the initial distribution as detailed in Sec. 2.3.2. However, this event generator does not include kinematic or chemical freeze-out mechanisms, which would characterize a complete simulation of the collision.

For all processes treated by PYTHIA, the program applies leading order results from p-QCD calculations, that is, it approximates the results to the first order that have non zero values. Contributions from higher order coefficients are generally included through parton radiations in the initial (ISR) and final state of the process (FSR). Also, the possible interactions done in PYTHIA are $2 \to 1$, $2 \to 2$ and $2 \to 3$, with more final objects meaning a more complex phase space for the generation procedure. Higher than two particles in the final stage have no generic treatment for the event generation process, and PYTHIA is currently optimized for the first two types of interactions.

Other aspects, such as colour reconnection, supersymmetric particles and beam remnants, are also included in the PYTHIA code, but were not explored in this project. For an in-depth discussion of these topics, see [35, 38].

2.3.2 The Lund fragmentation model

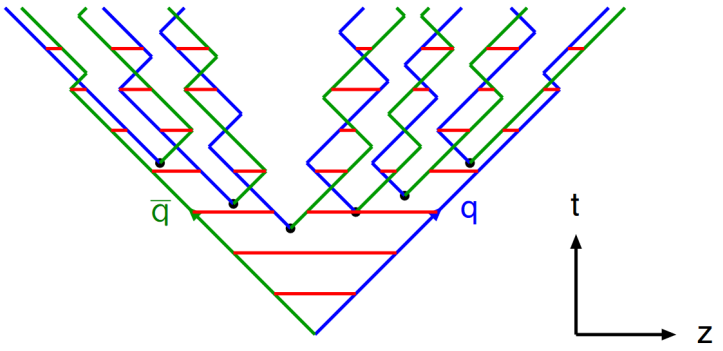

Figure 2.3: Motion of quarks and antiquarks in a $q'\bar{q}'$ system. Figure from "Monte Carlo Generators", lecture 2 (2006) [39].

To simulate the generation of hadronic matter, PYTHIA employs a model of string fragmentation for its simulation. In this model, hadronization takes place whenever a "string", a model for the flux of color between quarks and antiquarks in QCD, is fragmented. The essential condition for this to occur is that the effective potential from Eq. 1.2 have r large enough for it to be approximated as $V_{eff} \approx kr$, which is equivalent to indicate that such interactions will take place in the perturbative regime of quantum chromodynamics. As the potential increases with the distance, enough energy

may be available for the creation of a new $q'\bar{q}'$ pair. This color singled can, in turn, have enough energy to continue the string rupture process, ending when those strings have low enough energies to be considered, effectively, mesons. For baryons, the processes is similar but can result in unstable hadrons, which then may decay into other species of particles.

2.3.3 The Angantyr module

Aside from PYTHIA's use in the simulation of pp collisions, the newer versions of the code [38] also include a module responsible for the implementation of a model for heavy ions, making pA and AA simulations possible. The idea is similar to the TRENTo model, where the modelling of such collisions is done by combining several partons that corresponds to nucleon-nucleon collisions into a single heavy-ion event, which are then hadronized in the same fashion. The default option for this procedure in PYTHIA is called Angantyr [40].

In this model, it is important to note that special attention is given to the interaction between nucleons. In standard Glauber models, the only differentiation of the collision type is classifying those as an elastic or inelastic process. Here, the inelastic collisions are subdivided into single-diffractive, double-diffractive or non-diffractive events, which is achieved through a fluctuating nucleon-nucleon cross section. This contribution from diffraction is essential to model realistic cross-sections of heavy-ion collisions, as discussed in the model's implementation. The choice of the type of collision to be simulated is done by the principle of conservation of energy and momentum.

As for the treatment given for the interaction of the nucleus in each nuclei, the contributions of each to the total multiplicity of the event is inspired by Fritiof's approach [41], which was improved and detailed in Angantyr's implementation [40]. In it, this distribution is defined as

$$\frac{dN_{ch}}{d\eta} = w_t F(\eta) + w_p F(-\eta), \tag{2.5}$$

where $w_{p/t}$ is the number of participant nucleons for the projectile/target and $F(\eta)$ is the emission function of a single nucleus.

2.3.4 Generating an event

The stages for simulating a heavy-ion event can be summarized as follows,

1. The nuclei generated by the overlapping of protons, with its positions defined by a nucleon distribution function in the Angantyr module, go throught a projectile $\rightarrow$ target type of collision;

2. The number of participating nucleons is calculated by a Glauber model and then saved. As discussed in Sec. 2.3.3, the heavy-ion model also includes Angantyr's parametrizations for this stage;

3. An estimation of the final multiplicity of the event is done by Eq. 2.5;

4. Finally, the nucleon-nucleon sub-collisions and interactions are simulated through the Lund string model of Sec. 2.3.2, with its final hadronic state as the output.

Note that, as PYTHIA produces hadrons as an output, one could also implement a model consisting of only PYTHIA and a code package to simulate hadron cascades and decays in the freeze-out stage, resulting in a complete simulation that does not assume QGP production. This approach was recently developed by André Silva in this research group. The results of such methodology can be seen in [42].

2.4 Adapting PYTHIA's events to the simulation chain

As the resulting particles generated by PYTHIA described in the previous sections are not directly compatible with the expected parametrized $T^{\mu\nu}$ of hydrodynamics − which will be discussed in further detail in Sec. 3.1 − it is necessary to extract the information contained in these results and translate the given particle dynamics into continuous distributions of energy and momentum. Throughout this project, the approach implemented considered only the energy densities of each hadron, that is, $T^{\mu\nu} = T^{00} \neq 0$. An extension could be made, including the momenta to the initial conditions and filling the other components of the energy-momentum tensor. This will be latter discussed in Chap. 6.

2.4.1 The energy-momentum tensor as energy distributions

To effectively translate hadrons into initial conditions, one can start by filling the energy-momentum tensor with values given by a three-dimensional gaussian function

$$\boxed{\frac{1}{2\pi\sigma^2}\frac{1}{1+\exp\left(\frac{r-2\sigma}{a}\right)}\exp\left(-\frac{[(x-x_g)^2+(y-y_g)^2+(z-z_g)^2]}{2\sigma^2}\right)}. \tag{2.6}$$

In this equation, x, y and z are the positions of a given hadron extracted from the original outputs, x_g, y_g and z_g are the corresponding position of those hadrons in the grid where the $T^{\mu\nu}$ is calculated, with the range in each dimension used in this project being described below. Also, r is the ratius of

the nucleon, given by $r = \sqrt{(x - x_g)^2 + (y - y_g)^2 + (z - z_g)^2}$. The constant a is the thickness of the surface of the Pb nucleon, taken to be $a = 0.05$ fm given that the resolution of the grid is 0.1 fm. Finally, σ is the width of the gaussian function, set as $\sigma = 0.6$ fm based on the results shown in [43]. Notice that $\frac{1}{1+\exp\left(\frac{r-2\sigma}{a}\right)}$ comes from a Woods-Saxon distribution, used here to supress the gaussian tail that would otherwise appear at large values of r.

Two other restrictions must be implemented in the generation of such initial conditions, namely the selection of transverse momenta below 5.0 GeV/c and energies lower than 5.0 GeV. The reason for such cutouts is that, not only are highly energetic particles very rare, but they conflict and are a source of errors for the code package used in the simulation of the hydrodynamic stage.

With Eq. 2.6, it is then possible to calculate a hadron-by-hadron distribution of the energies and write the results into the grid representing the energy-momentum tensor. The parameters used for this end were the ranges of $[-14, 14]$ fm to x and y and $[-10, 10]$ fm to z. The two-dimensional case projected the contents of this latter plane, which means for Eq. 2.6 to take $z = z_g = 0$. Also, the code was designed to be able to save some parameters of interest of the events, such as the original impact parameter, number of participants and centrality.

For the computational aspects of the implementation of those initial conditions through PYTHIA, the HadrEx class, a code package developed in the group were this research was done, was employed. As this class is able to extract information from PYTHIA's output, such as the hadron position, momenta, energy and many others, it was essential to the development of the initial conditions used in this work. This framework was also used to perform analysis on the outputs of the simulation chain, which will be discussed latter in Sec. 3.2.3.

Hydrodynamics and the simulation

In this chapter, some relevant aspects of the hydrodynamic evolution will be presented and discussed. First, as an introduction, the theoretical modeling of a viscous fluid will be done on Sec. 3.1, where the time evolution of the energy-tensor of the previous chapter will also be discussed. In Sec. 3.2, the computational aspects and the basic principles of the simulation chain are shown. The last stage, described in Sec. 3.3, will give a brief overview of the anisotropy generated by the evolution of the fluid, with its respective calculations done in the next chapter, on Sec. 4.2.

3.1 Characterizing viscous hydrodynamics

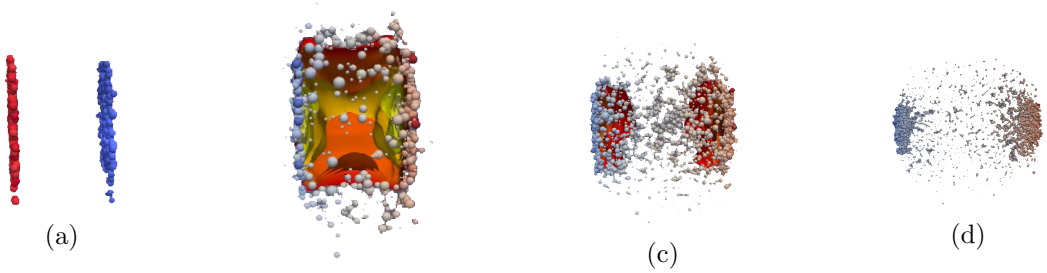

(a) (b) (c) (d)

Figure 3.1: (a). Instants before the collision event, showing a head-on configuration. (b) Formation of the QGP from the initial density. (c) Particlization process. (d) Hadronic cascade, where the freeze-out processes takes place. Figures from [44].

As mentioned in Sec. 2.4, an initial condition for hydrodynamics is the representation of the energy-momentum tensor and encompasses all the properties of the initial density generated by a given collision. This tensor is composed of four different fields, as shown below in Eq. 3.1.

$$T^{\mu\nu} = \epsilon u^{\mu} u^{\nu} - (P_0 + \Pi)\Delta^{\mu\nu} + \pi^{\mu\nu}. \tag{3.1}$$

Above, ϵ is the energy density in the local rest frame of the fluid, u^{μ} maps the flow velocity of the fluid, $\pi^{\mu\nu}$ is the stress tensor, Π the bulk pressure and the initial pressure, $\mathrm{P}_0 = \mathrm{P}_0(T, \mu_b, \mu_e, \mu_s)$, is connected to the energy distribution through the equation of state (EoS). Energy-momentum and net-charge conservation in the fluid imply in the following equations for $T^{\mu\nu}$ and N^{μ}, where N^{μ} the

net-charge 4-current of the plasma:

$$\partial_\mu T^{\mu\nu} = 0 \quad , \quad \partial_\mu N^\mu = 0. \tag{3.2}$$

The difference between viscous and non-viscous (or ideal) dynamic lies in the parameters $\pi^{\mu\nu}$ and Π, in which both are taken to be zero in ideal fluid approximation. This equation can then be rewritten as

$$T^{\mu\nu} = \epsilon u^\mu u^\nu - P(g^{\mu\nu} - u^\mu u^\nu), \tag{3.3}$$

and, to solve such equations, the methodology will assume the flow velocity to be the unit vector satisfying

$$T^\mu_\nu u^\nu \equiv \epsilon u^\mu \quad , \quad u^\mu u_\mu = 1. \tag{3.4}$$

For the modeling employed in phenomenological models, the conservation of energy and equation of state are complemented by the equations of motion of the shear stress tensor $\pi^{\mu\nu}$, and those of the bulk pressure Π. The physics of such equations and its implementation on MUSIC, the code package of choice for this stage, is discussed in [45–47]. This procedure assumes the 14-moments approximation for Israel-Stewart-type equations of second-order viscous hydrodynamics. Those can be written in a compact manner by

$$\begin{aligned}\tau_\pi \dot{\pi}^{\langle\mu\nu\rangle} + \pi^{\mu\nu} = 2\eta\sigma^{\mu\nu} + 2\tau_\pi \pi_\alpha^{\langle\mu}\omega^{\nu\rangle\alpha} - \delta_{\pi\pi}\pi^{\mu\nu}\theta + \varphi_\tau \pi_\alpha^{\langle\mu}\pi^{\nu\rangle\alpha} \\ - \tau_{\pi\pi}\pi_\alpha^{\langle\mu}\sigma^{\nu\rangle\alpha} + \lambda_{\pi\Pi}\Pi\sigma^{\mu\nu} + \varphi_6\Pi\pi^{\mu\nu},\end{aligned} \tag{3.5}$$

for the shear stress tensor and

$$\tau_\Pi \dot{\Pi} + \Pi = -\zeta\theta - \delta_{\Pi\Pi}\Pi\theta + \varphi_1\Pi^2 + \lambda_{\Pi\pi}\pi^{\mu\nu}\sigma_{\mu\nu} + \varphi_3\pi^{\mu\nu}\pi^{\mu\nu}, \tag{3.6}$$

for the bulk pressure.

The two first-order coefficients, that are normally given by empirical equations, are the shear viscosity η and bulk viscosity ζ. Also, the other coefficients, of second-order, are τ_π, $\delta_{\pi\pi}$, φ_τ, $\tau_{\pi\pi}$, $\lambda_{\pi\Pi}$, φ_6, τ_Π, $\delta_{\Pi\Pi}$, φ_1, $\lambda_{\Pi\pi}$ and φ_3, also given by parametrizations (see [48]). Those transport coefficients are characteristics of the response of the QGP to deviations from equilibrium.

3.2 The simulation chain

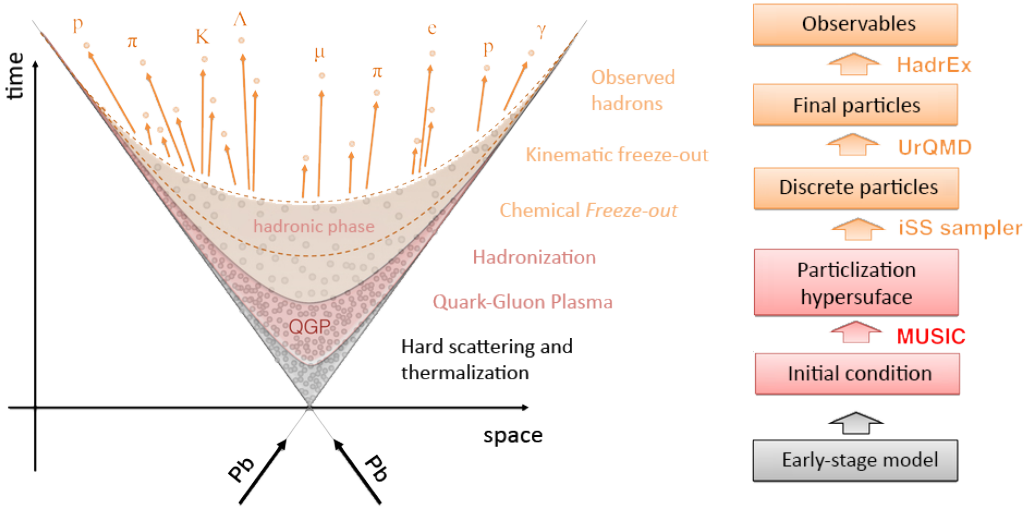

Figure 3.2: Stages of a hydrodinamic evolution. The graph on the left shows the physical aspects of such evolution, and the boxes to the right the code packages employed in each corresponding stage.

3.2.1 Applying hydrodynamics

In the thermalization stage of the QGP, the MUSIC package has the task of describing the relativistic hydrodynamic evolution of the previously given initial conditions. With the appropriate equations of state (EoS), given by either a parametrization or a numeric table, MUSIC can then numerically solve Eq. 3.1 using hyperbolic coordinates and save the resulting fluid for latter stages. The chosen equation of state for the evolution of the system was generated to match HotQCD lattice calculations of s-QGP and include the hadron resonance gas contributions of [49], with its source code found on [50]*. For more information on recent research related to modeling equations of state for strong coupled QGP, see [51].

In this stage, many variables must be properly defined in order to create a hydrodynamic evolution. As shown in Sec. 3.1, the energy-momentum tensor is described by the characteristics of the fluid, which in turn is given by its viscosity parameters. Also, defining the initial τ and total time τ_f for the hydrodynamic evolution, with a freeze-out temperature given by T, are equally important. Thus, the methodology used to implement such parametrizations in this work is described below:

- Both shear (η) and bulk (ζ) viscosities are given, respectively, by Eqs. 4 and 5 of [49] and their

*The specific code to generate the EoS used in this project from this source was: `python3 eos.py --res-width-off --species=urqmd --Tmax 1.0 --write-bin eos_urqmd.bin --music_output_format`

respective parameters;

  - Many other parametrizations could be employed to this model. However, as these choices were made for the baseline TRENTo model, they were also applied here;
  - $(\eta/s)_{hrg}$ is a parameter correlated to the hadron resonance gas and also discussed in [49]. As the range of possible values is considerably high, an estimation was done via Fig. 13 from [52], using the window of temperature between the transition to QGP ($T_c = 0.154$ MeV) and freeze-out of the surface as an approximation.

- Following the discussion done in Sec. 5.1.3, τ was taken here to be 1.7 fm/c, allowing the use of all hadrons produced by the PYTHIA event generator;
- Considering that central collisions may take more time to evolve, τ_f was chosen to be 30 fm/c as a superior limit;
- The freeze-out temperature for the chosen parametrization is given by $T = 0.148$ MeV, with the method used for its calculation described in [53].

It is important to note that the parameters for these equations where tuned with a two-dimensional approach in mind, and as such, three-dimensional hydrodynamic evolution may diverge from the expected experimental results as a consequence. The task of retuning those parameters to account for 3D initial conditions is feasible, but will demand a large amount of computational resources to be accomplished.

Also, as a technical note, running this hydrodynamic evolution through MUSIC has a high computational cost and is time consuming. To remedy this issue, a technique known as oversampling is performed in the outputs given by this program, generating several events that are later evolved by the remaining modules of the chain. The number of particles used for each approach will be given in the next section.

3.2.2 Hadronization and particlization

It is essential that the hydrodynamic stage ends with a well defined criteria, as this point defines the transition of a hypersurface, generated by the evolution of the energy-momentum tensor, into hadrons (hadronization) and then final particles (particlization). This process happens at a given temperature or energy density, through the equation of state, ranging from 150 to 200 MeV, in which

the phase transition of the QGP to confined matter occurs. The evolution is considered complete if all points in the system are below the said criteria.

The Cooper-Frye formula [54], as shown below, is used to model this phase transition. The main characteristic of this stage is the free propagation of particles, decoupled from the previous collective behavior of the system as a consequence of its expansion.

$$E\frac{d^3N_s}{dp^3} = g_s \int_\Sigma d\Sigma_\mu P^\mu f_s(P, \epsilon, u^\mu, \pi^{\mu\nu}, \Pi), \tag{3.7}$$

where $E\frac{d^3N_s}{dp^3}$ is the distribution of energy and momentum of each produced hadron.

This approach splits the freeze-out process into two different stages, from which the transition detailed previously may occur. First, its chemical phase, with T_{ch} as the defined temperature criteria to the transition, in which the inelastic scattering of hadrons ceases, creating a constant density of species of particles; and the kinetic phase, starting at $T_{kin} < T_{ch}$, ending the elastic scattering of those hadrons. Here, Cooper-Frye's equation only accounts to the chemical freeze-out stage, with its numerical solution being performed by the iSS package.

In the same way done for the hydrodynamic evolution, this package also needs several variables to run its simulation, with those given by

- The Cooper-Frye formula (Eq. 3.7) must include corrections for the function f_s, that is, $f_s = f_0 + \delta f$, with only shear viscosity corrections being used for the viscous correction. Neglecting the bulk contribution (δf_{bulk}) was done given that ζ/s is small at the particlization stage [49];

- Using a sampling method, as mentioned before, which was done using a Poisson distribution to sample the whole distribution of particles in rapidity (dN/dy). The number of hadrons to sample was set to 50.000 (500.000) in the two dimensional (three-dimensional) simulation;

  - The windows of rapidity and pseudorapidity for sampling were set to, respectively, $|y| < 5.0$ and $|\eta| < 0.8$, to match experimental data, while the range of transverse momenta was set as $p_T < 5.0$ GeV/c.

Also, some of the choices for the previous stage, such as the 14-moments approximation, viscous characterization of the fluid, boost invariance or corrections and more, were carried to iSS in its input file.

The parameters discussed above are such that the output given by iSS does not include all the physical description of the evolution of particles, as the remaining interactions and decays are not included in this stage. For that reason, the UrQMD package will then be employed into the chain, with its basic aspects covered in the next section.

3.2.3 Interactions and decay

The previous sections describes the transition of the QGP fluid into hadronic degrees of freedom, where a gas of hadrons is formed. These hadrons, however, continue to interact, up to the kinectic freeze-out temperature T_{kin} mentioned before, and decay into multiple species. This second stage of particlization, that completes the physical description of the process, is done by UrQMD package, which describes the dynamics of the observables byproducts of the collision chain, using a transport model and the outputs given in the earlier stages of the simulation. The documentation of the code and more information on its procedure can be found on [55].

3.2.4 Analysis of the simulation results

After the evolution done in iSS and UrQMD ends, its outputs must then be analysed. This was done using the HadrEx class, the same applied also in Sec. 2.4.1, which is able to retrieve all information of the observables produced, creating a framework that is useful in the writing of analysis code and in extracting graphical information from those results.

However, specifically for the outputs given by UrQMD, the information contained in its `.OSCAR` files must first be made compatible to the HadrEx class framework. This is done by the use of conversion programs also developed in the group.

3.3 Anisotropic flow

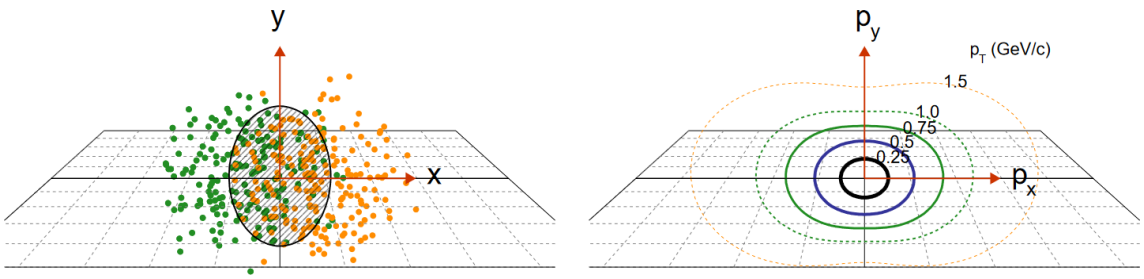

Figure 3.3: Left: a schematic representation of a non-central collision. Right: the profile of the surface modeled by the v_2 coefficient, with each average radius representing the p_T of the particles and the anisotropy of the ring indicating the magnitude of the elliptic flow coefficient. Figure from [56].

As described in Sec. 1.1.2, an interesting phenomenon observed in experimental measurements of heavy-ion collisions is a rather collective behavior of the produced particles, which can be verified by the anisotropic configuration of those particles. This observed distribution can be understood as a consequence of the spatial anisotropy of the initial density of the system, which in turn is converted into momentum anisotropy that can be measured through correlations of the final particles.

First, note that the anisotropy can be estimated from the momentum distribution of the particles. This can be quantified, as shown in [57], using a Fourier series

$$E\frac{d^3N}{d^3p} = \frac{1}{2\pi p_t}\frac{d^2N}{d\eta dp_t}\left(1 + \sum_{n=1}^{\infty} 2v_n cos(n[\phi - \Psi_{RP}])\right), \tag{3.8}$$

where $E\frac{d^3N}{d^3p}$ is analogous of the same distribution from Eq. 3.7. The differential coefficients v_n of the series, usually functions of transverse momentum and rapidity of the particles, are given by

$$v_n = \langle cos(n[\phi - \Psi_{RP}])\rangle, \tag{3.9}$$

with $\langle ...\rangle$ denoting the mean taken first onto the initial subset of particles in each event and, after that, calculated over all events. The angular variables ϕ and Ψ_{RP} define, in this order, the azimuthal angle and the reaction plane angle. Also, n defines the nth coefficient of the series, where the first three coefficients, v_1, v_2, v_3, are designated, respectively, as directed flow, elliptic flow and triangular flow. It is also important to note that the last two react to different types of asymmetry in the event plane. Shown above in Fig. 3.3 is a representation of the momentum anisotropy of the final distribution of particles to the observed elliptic flow. Note that the initial geometry of the collision is essentially elliptic.

This figure also contains qualitative information on the impact of E into the anisotropy of the system. As the collision energy increases, so does the gradients observed in the right-side image of 3.3, and consequently the resulting distribution of particles, and the geometry of their collective behavior, is altered by this parameter. In all simulation results presented in Chap. 5, the collision energy in the center of mass frame is set as $\sqrt{s_{\mathrm{NN}}} = 2.76$ TeV.

Experimental observables

This chapter aims to provide an overview of the variables and distributions used to study the simulation outputs, which also allows for a comparison with the available experimental results. Sec. 4.1 will discuss the distribution of particles as functions of experimental observables and Sec. 4.2 details the calculations performed to extract flow coefficients, with a connection of those with eccentricities done in Sec. 4.2.1.

4.1 The distribution of produced particles

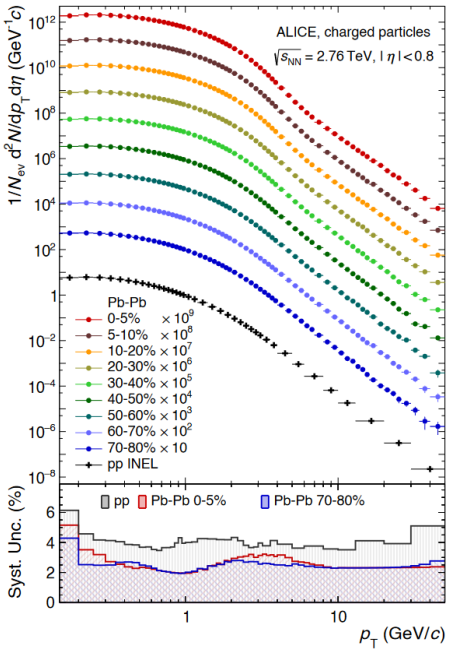

(a)

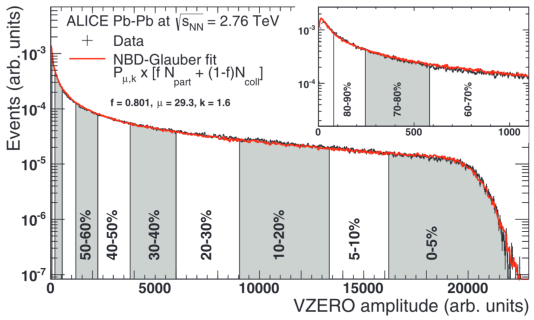

(b)

Figure 4.1: (a) Transverse momenta distribution of charged particles resulting from Pb-Pb collisions, for $|\eta| < 0.8$ and $\sqrt{s_{NN}} = 2.76$. Figure from [58]. (b) Distribution of multiplicity for charged particles, arbitrary units, with its convolutional fit shown in red. Figure from [25].

To begin measuring the characteristics of the resulting hadrons and set a baseline for the subsequent analysis, one can measure the number of observed charged particles as a function of their kinematic variables, such as transverse momenta, as shown in Fig. 4.1. Note that some of the results presented

in Chap. 5 shows, for example, distributions using the mean p_T and as a function of centrality, which is useful to verify the whole spectra with respect to another variable.

In accelerator experiments, the multiplicity of resulting particles can also be obtained while adjusting the obtained data by a Monte Carlo calculation, done by a convolution of a negative binomial distribution (NBD) and a linear combination of the number of participants N_{part} and colliding nucleons N_{coll}, named number of ancestors N_{anc}, which accounts for both contributions in a heavy-ion collision. The idea of such convolution is to use the NBD as a model of multiplicity for the Pb-Pb events and combine those to the N_{anc} contributions.

The definition used to perform those calculations is $P_{\mu,k} * N_{anc}$, where

$$P_{\mu,k}(n) = \frac{\Gamma(n+k)}{\Gamma(n+1)\Gamma(k)} . \frac{(\mu/k)^n}{(\mu/k)^{n+k}}, \tag{4.1}$$

and the linear combination is defined as

$$N_{anc} = fN_{part} + (1-f)N_{coll}, \tag{4.2}$$

with f as a fraction of participants considered, being 0.801 for Pb-Pb collisions at 2.76 TeV [59] as shown also in Fig. 4.1.

Also, another characteristic of produced particles can be quantified when considering their angular distribution, which will also be useful for the development of anisotropy discussions in the next section. From Eq. 3.8, the azimuthal dependence of this final particle distribution can be written as

$$\frac{2\pi}{N}\frac{dN}{d\phi} = 1 + \sum_{n=1}^{\infty} 2v_n cos(n[\phi - \Psi_{RP}]) = \sum_{n=-\infty}^{\infty} v_n e^{in\Psi_n} e^{-in\phi}. \tag{4.3}$$

Notice that this equation also helps to define the phase of the Fourier coefficients through v_n and the reference angle for each harmonic n. That is,

$$\langle e^{n\phi} \rangle = v_n e^{in\Phi_n}. \tag{4.4}$$

This quantity will latter be used in Sec. 4.2.1 to correlate the eccentricities of initial conditions to the anisotropic flow.

4.2 Quantifying anisotropic flow using cumulants

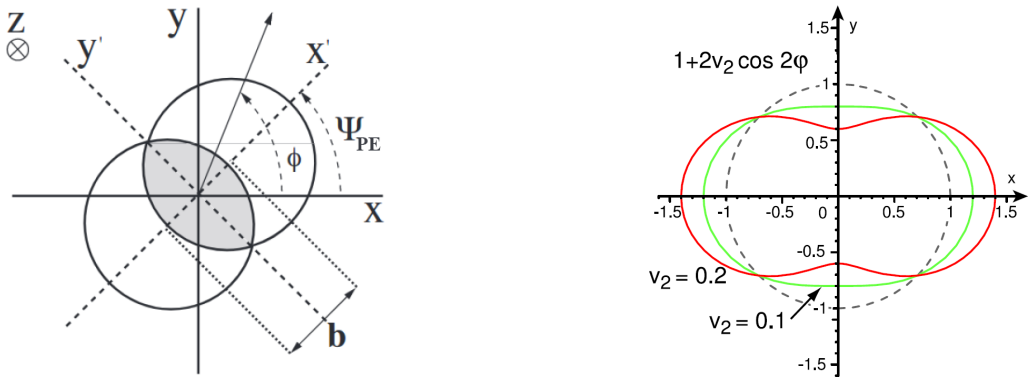

Figure 4.2: (a) Representation of the angle of a particle ϕ with respect to the event plane S. (b) Visual representation of the elliptic flow's amplitude. The dotted line corresponds to $v_2 = 0$.

Having defined the flow coefficients in Eq. 3.9, their numeric calculation can be done through two approaches: using the event plane method, with the event plane angle Ψ_{RP} being another variable only available for simulation techniques; or the cumulant method. This work will focus only on the study done through the latter, as it also has the advantage of determining the correlation between observed particles.

The essential aspect of the cumulant method is that it can be defined as a technique that determines those particle correlations by analysing the global anisotropy of an event, which is in turn a result of the initial stages of the collision. The main hypothesis is that, if each particle is somehow correlated to this global anisotropy, then those will also have a angular correlation between themselves. This also leads to an interesting connection to the eccentricity of an event, which will be discussed latter in Sec. 4.2.1.

Extracting such coefficients will be restricted to second and fourth order correlations, with higher order results given in [60]. Increasing the order of particle correlations turns the results less sensitive to local correlations, resulting in, for example, the two-particle correlation of the second harmonic ($n = 2$ in Eq. 3.9), $v_2\{2\}$, being the best choice to study a local phenomena, such as connections from particle decays. Thus, higher order on n of this same harmonic, as in $v_2\{4\}$, is more fit to observe the global aspect of particle emission.

The technique used to perform such calculations is named Q-cumulant method. The implementation into the analysis macro is relatively simple, and avoids a potential issue with encased loops that is also a computationally efficient way of calculating cumulants. Starting from the definition of the

Q-vector for an given harmonic of nth order, Q_n, as shown below in Eq. 4.5,

$$Q_n = \sum_{i=1}^{M} e^{in\phi_i}, \quad \begin{cases} |Q_n|^2 = \sum_{i,j=1}^{M} e^{in(\phi_i - \phi_j)} = M + \sum_{i,j}^{'} e^{in(\phi_i - \phi_j)} \\ |Q_n|^4 = Q_n Q_n Q_n^* Q_n^* = \sum_{i,j,k,l=1}^{M} e^{in(\phi_i + \phi_j - \phi_k - \phi_l)} \end{cases}, \tag{4.5}$$

where M is the multiplicity, ϕ the angles and the sum $\sum^{'}$ must be done for different indexes. The mean of the correlations for two and four particles, in this order, for each event, can then be defined as

$$\langle 2 \rangle = \langle e^{in(\phi_1 - \phi_2)} \rangle = \frac{1}{P_{M,2}} \sum_{i,j}^{'} e^{in(\phi_i - \phi_j)} = \frac{|Q_n|^2 - M}{M(M-1)}, \tag{4.6}$$

$$\begin{aligned} \langle 4 \rangle = \langle e^{in(\phi_1 + \phi_2 - \phi_3 - \phi_4)} \rangle = \frac{1}{P_{M,4}} \sum_{i,j,k,l}^{'} e^{in(\phi_i + \phi_j - \phi_k - \phi_l)} = \\ = \frac{|Q_n|^4 + |Q_{2n}|^2 - 2\Re|Q_{2n} Q_n^* Q_n^*|}{M(M-1)(M-2)(M-3)} - 2\frac{2(M-2).|Q_{2n}|^2 M(M-3)}{M(M-1)(M-2)(M-3)}, \end{aligned} \tag{4.7}$$

where $P_{n,m} = n!/(n-m)!$.

Now, taking the mean over the events, one arrives at

$$\langle\langle 2 \rangle\rangle = \langle\langle e^{in(\phi_1 - \phi_2)} \rangle\rangle = \frac{\sum_{events} (W_{\langle 2 \rangle})_i \langle 2 \rangle_i}{\sum_{events} (W_{\langle 2 \rangle})_i}, \tag{4.8}$$

$$\langle\langle 4 \rangle\rangle = \langle\langle e^{in(\phi_1 + \phi_2 - \phi_3 - \phi_4)} \rangle\rangle = \frac{\sum_{events} (W_{\langle 4 \rangle})_i \langle 4 \rangle_i}{\sum_{events} (W_{\langle 4 \rangle})_i}, \tag{4.9}$$

where $W_{\langle 2 \rangle}$ and $W_{\langle 4 \rangle}$ are used to minimize the effects of the multiplicity fluctuation in each event, with

$$W_{\langle 2 \rangle} = M(M-1), \tag{4.10}$$

$$W_{\langle 4 \rangle} = M(M-1)(M-2)(M-3). \tag{4.11}$$

Notice that the same coefficients defined by Eqs. 4.10 and 4.11 appear, respectively, on the

denominators of Eq. 4.6 and 4.7.

Now, with those definitions given, it is possible to define the cumulant coefficients for the events and arrive at the flux coefficients,

$$\boxed{c_n\{2\} = \langle\langle 2\rangle\rangle \Rightarrow v_n\{2\} = \sqrt{c_n\{2\}}}, \tag{4.12}$$

$$\boxed{c_n\{4\} = \langle\langle 4\rangle\rangle - 2.\langle\langle 2\rangle\rangle^2 \Rightarrow v_n\{4\} = \sqrt[4]{-c_n\{4\}}}. \tag{4.13}$$

Finally, the differential flow coefficients for two and four particle correlations can be calculated, which are actual measured variables in heavy-ion collisions. Their final form is given by the following relations

$$\boxed{d_n\{2\} = \langle\langle 2'\rangle\rangle \Rightarrow v'_n\{2\} = \frac{d_n\{2\}}{\sqrt{c_n\{2\}}}}, \tag{4.14}$$

$$\boxed{\langle\langle 4'\rangle\rangle - 2.\langle\langle 2'\rangle\rangle^2 \Rightarrow v'_n\{4\} = \frac{d_n\{4\}}{(-c_n\{4\})^{3/4}}}. \tag{4.15}$$

where $d_n\{2\}$ and $d_n\{4\}$ are, respectively, the coefficients of second and fourth order for particle detectors with uniform azimuthal acceptance, being this the case for the simulated events in this project. To arrive at Eqs. 4.14 and 4.15, it is first necessary to define the quantities vector-p and vector-q

$$\begin{cases} p_n = \sum_{i=i}^{m_p} e^{in\psi_i} \\ q_n = \sum_{i=i}^{m_q} e^{in\psi_i} \end{cases}, \tag{4.16}$$

where p_n encases particles with some characteristic (or characteristics) of interest, such as intervals of p_T or rapidity, denoted as *Particle of Interest* (POI), and q_n refers to particles used in the calculations of the reference flux, known as *Reference Flow Particle* (RFP). This coefficient also subtracts effects of self correlation.

With that done, $\langle\langle 2'\rangle\rangle$ and $\langle\langle 4'\rangle\rangle$ will then be calculated by taking the same two means as before (by event and for all events) and rewritten using the Q-vector, q-vector and p-vector formalism

$$\langle 2' \rangle = \langle e^{in(\phi_1 - \phi_2)} \rangle = \frac{1}{m_p M - m_q} \sum_{i=1}^{m_p} \sum_{j^*=1}^{M} e^{in(\phi_i - \phi_j)} = \frac{p_n Q_{n^*} - m_q}{m_p M - m_q}, \tag{4.17}$$

$$\begin{aligned} \langle 4' \rangle = \langle e^{in(\phi_1+\phi_2-\phi_3-\phi_4)} \rangle = \frac{1}{(m_p M - 3m_q)(M-1)(M-2)} \sum_{i=1}^{m_p} \sum_{j^*,k^*,l^*=1}^{M} e^{in(\phi_i+\phi_j-\phi_k-\phi_l)} = \\ = (p_n Q_n Q_n^* Q_n^* - q_{2n} Q_n^* Q_n^* - p_n Q_n Q_{2n}^* - 2M p_n Q_n^* - 2m_q |Q_n|^2 + 7 q_n Q_n^* - Q_n q_n^* \\ q_{2n} Q_{2n}^* + 2 p_n Q_n^* + 2 m_q M - 6 m_q)/[(m_p M - 3m_q)(M-1)(M-2)], \end{aligned} \tag{4.18}$$

Using then

$$w_{\langle 2' \rangle} = m_p M - m_q, \tag{4.19}$$

$$w_{\langle 4' \rangle} = (m_p M - 3m_q)(M-1)(M-2), \tag{4.20}$$

as weights for the following relations, one arrives at

$$\langle\langle 2' \rangle\rangle = \langle\langle e^{in(\phi_1 - \phi_2)} \rangle\rangle = \frac{\sum_{events} (W_{\langle 2' \rangle})_i \langle 2' \rangle_i}{\sum_{events} (W_{\langle 2' \rangle})_i}, \tag{4.21}$$

$$\langle\langle 4' \rangle\rangle = \langle\langle e^{in(\phi_1+\phi_2-\phi_3-\phi_4)} \rangle\rangle = \frac{\sum_{events} (W_{\langle 4' \rangle})_i \langle 4' \rangle_i}{\sum_{events} (W_{\langle 4' \rangle})_i}, \tag{4.22}$$

which results in Eqs. 4.14 and 4.15. For the initial proposal of the method and a greater level of detail on its development, see [61].

4.2.1 Connecting flow and the initial distribution

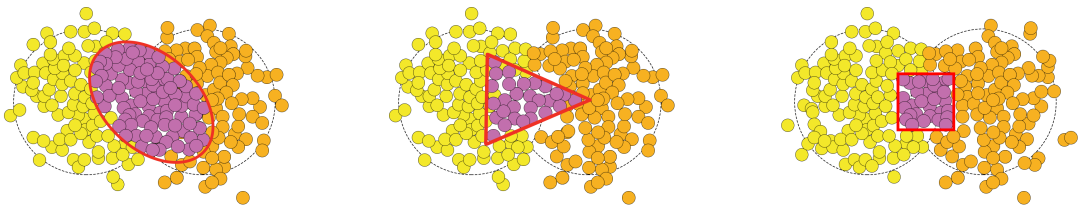

(a) (b) (c)

Figure 4.3: (a) Eccentricity, ϵ_2. (b) Triangularity, ϵ_3. (c) Quadrangularity, ϵ_4, with the flow occurring in the perpendicular direction to the red contour of each figure. Inspired by [62].

To better understand the different distributions of anisotropic flow of observables, a connection to

the original anisotropy of the density distribution can be made. That is, it is possible to correlate the different eccentricities of a collision to the resulting collective behavior of particles. To do so, take the two-dimensional Fourier transform of the transverse density $\rho(\mathbf{x})$ of the participant nucleons,

$$\frac{\rho(\mathbf{k})}{\rho(0)} = \frac{\int d^2x \rho(\mathbf{x}) e^{ik.x}}{\int d^2x \rho(\mathbf{x})}, \tag{4.23}$$

with $\rho(0)$ being the density given in the center of the reference frame. Now, expanding this results in harmonics and in powers of $k \equiv \sqrt{\mathbf{k}^2}$ as in [62],

$$\frac{\rho(\mathbf{k})}{\rho(0)} = \sum_{n=-\infty}^{\infty} \sum_{m=0}^{\infty} \frac{i^m}{m!} \varepsilon_{m,n} k^m e^{-in\phi_k}, \tag{4.24}$$

where the polar coordinates were used and

$$\varepsilon_{m,n} = \frac{m!}{2^m \left(\frac{m+n}{2}\right)! \left(\frac{m-n}{2}\right)!} \langle r^m e^{in\phi} \rangle \quad , \quad \langle \dots \rangle = \frac{\int d^2x \rho(\mathbf{x}) \dots}{\int d^2x \rho(\mathbf{x})}, \tag{4.25}$$

with the moments $\varepsilon_{m,n}$ being non-zero for $m \geq |n|$ and $(m-n)$ being even. A coordinate system such that $\langle x \rangle = \langle y \rangle = 0$ will also be used for posterior calculations.

As noted in the last section, the anisotropic flow is less sensitive to local correlations of particles of higher order, which is equivalent to say that the contributions of higher-order in k for the momenta will be not as relevant than the lower order contributions. This is also a consequence of the hydrodynamic approach, where its long-wavelength description is only valid if the dynamics for short distances can be neglected.

With that in mind and noting that $\varepsilon_{2,0} \propto \langle r^2 \rangle$ and $\varepsilon_{2,2} \propto \langle r^2 e^{2i\phi} \rangle$, the second order spatial momentum is [62, 63]

$$\epsilon_2 = -\frac{\langle r^2 e^{2i\phi} \rangle}{\langle r^2 \rangle}, \tag{4.26}$$

which is consistent with Eq. 2.2.

This ratio quantifies the ellipticity for the flow of particles, and as such must be proportional to the previous definitions of elliptic flow, that is, $v_2 \propto \epsilon_2$. For smooth initial conditions − those with continuous gradients of energy and momentum on the original density distribution − Eq. 4.26 predicts the resulting anisotropy of the simulated events, but is also a reasonable approximation for general densities [62]. The higher order corrections will be given by the degree of m in Eq. 4.25.

Results

Following previous discussions, this chapter will present a variety of results from the performed simulations, from both two-dimensional and three-dimensional setups for initial conditions and their resulting observables. Sec. 5.1 contains the geometric characterization of the initial distributions generated by the methodology described in Sec. 2.4. Sec. 5.2, on the other hand, will use the procedure described in Chap. 4 to quantify the resulting particles with respect to variables of interest.

Whenever possible, the results of this project will be compared to those from the experimental data from the ALICE collaboration, with the pseudorapidity interval for simulated results taken to be $|\eta| < 0.8$, unless explicitly mentioned to have a different value, as to match the experimental data available.

5.1 Characterizing an initial condition

5.1.1 Geometric properties

Along Sec. 2.4, the steps to translate the generated outputs from PYTHIA's simulations into initial densities of energy contained in the elements of the energy-momentum tensor $T^{\mu\nu}$ were described, which allowed for the posterior hydrodynamic evolution of such densities. It is essential to characterize those distributions with respect to their geometry, knowing that these properties will impact on the resulting observables from the simulation chain, while also proving useful information on the physical aspects of this model.

An immediate result from using Eq. 2.6 to model the expected densities is the observed profile of those initial conditions. In Figs. 5.1-5.3, showing central, semi-central and peripheral events in this order, the two-dimensional version of Eq. 2.6 was used to produce the distributions used in the 2D hydrodynamic simulations, and in those figures a comparison to TRENTo's outputs for the equivalent centralities was also made to define a baseline for this study.

Notice that, in all figures, the maximum magnitude of the distributions is similar, with the model employing PYTHIA's approach generating more *hotspots*, that is, local high-density spots, than its

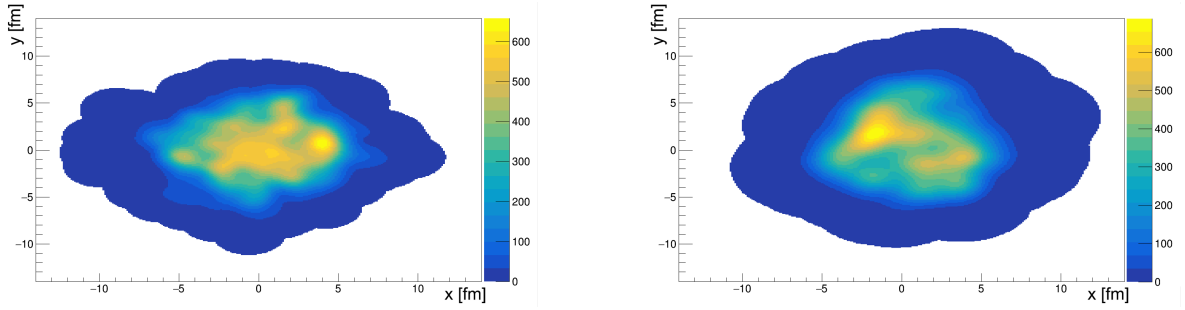

(a) (b)

Figure 5.1: Comparison between density profiles for the centrality $0-5\%$. (a) Results from converting PYTHIA events and (b) TRENTo's output.

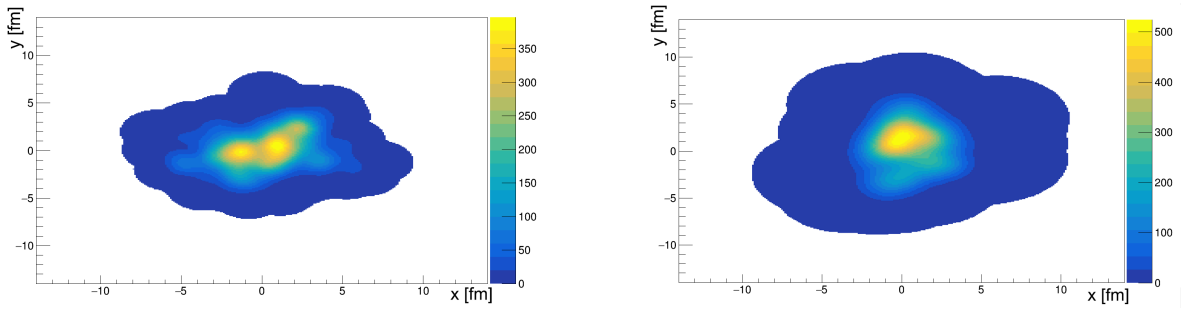

(a) (b)

Figure 5.2: Comparison between density profiles for the centrality $40-50\%$. (a) Results from converting PYTHIA events and (b) TRENTo's output.

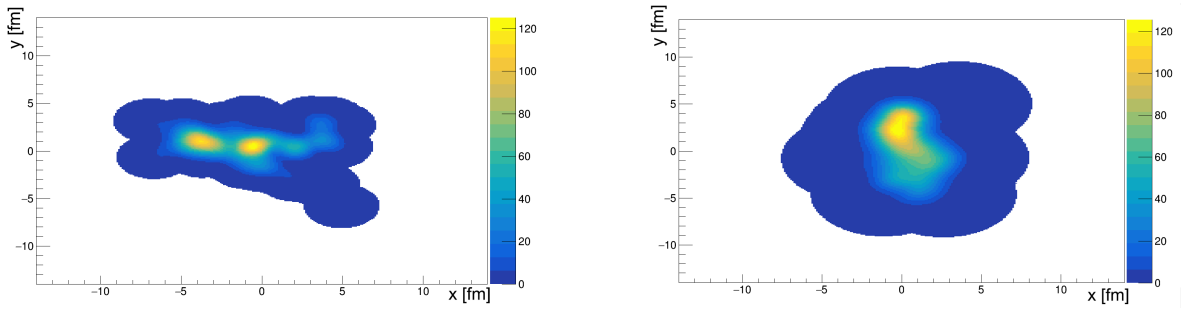

(a) (b)

Figure 5.3: Comparison between density profiles for the centrality $70-80\%$. (a) Results from converting PYTHIA events and (b) TRENTo's output.

parametric counterpart, which presents a smoother distribution of densities. As pointed in Sec. 2.3.1, the former model does not create a superior limit to the energies or momenta of the generated particles − done manually in the conversion stage by setting $p_T < 5.0$ GeV/c and $E < 5.0$ GeV as an acceptance window for hadrons −, allowing outliers to be relevant and in turn generating higher gradients of energy in the resulting density.

The previous discussion indicates that PYTHIA might produce a very different geometric structure

for those initial conditions. To quantify this effect, Eq. 4.25 was used to obtain the eccentricity (ϵ_2), triangularity (ϵ_3) and quadrangularity (ϵ_4) of such initial conditions, with the results shown below on Figs. 5.4.

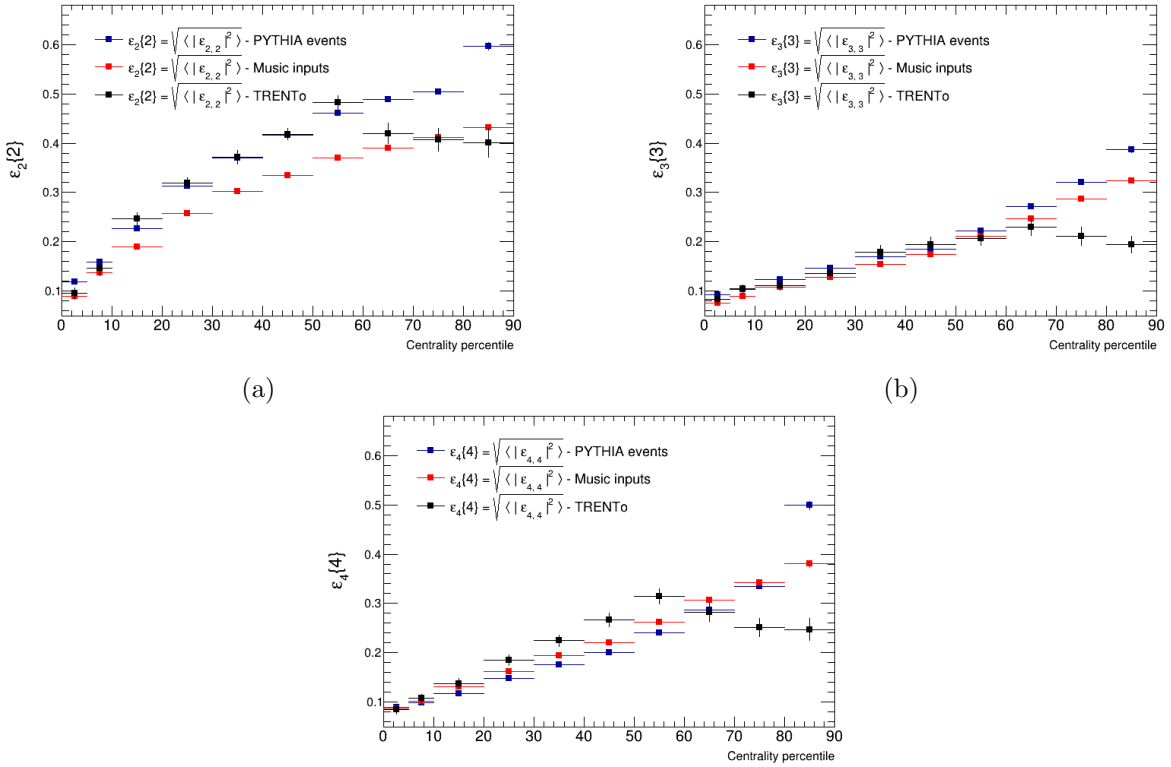

Figure 5.4: Eccentricity coefficients of simulated events, with PYTHIA's output results shown in blue, the initial density generated using those events plotted in red and the baseline, TRENTo, in black. (a) eccentricity (ϵ_2), (b) triangularity (ϵ_3) and (c) quadrangularity (ϵ_4).

Notice that there is a clear divergence for peripheral events ($50 - 60\%$ in centrality) between the behavior of the PYTHIA model and TRENTo's approach. Those differences indicate that the spatial distribution of the nucleons modeled by those initial conditions are intrinsically distinct for those centralities: while the parametric model defines an elliptic-like distribution, PYTHIA presents higher contributions on higher centralities, and thus having a lump-like substructure.

In the three-dimensional approach, the initial conditions were formulated using the η_s (Z) component of each produced particle as a third dimension. The best way to extract qualitative information on the energy distributions is to define projections on a plane from the original profile, as done in Fig. 5.5 using the XY and ZY planes.

From those figures and comparing them to the previous two-dimensional initial conditions, one

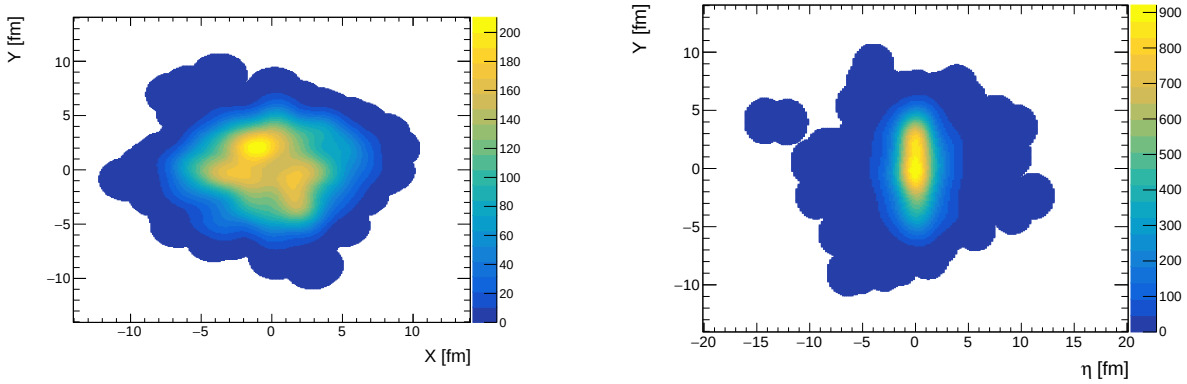

(a) (b)

Figure 5.5: Projections of a three-dimensional initial condition produced using Eq. 2.6 and PYTHIA's events, for the range of 0-10% in centrality. (a) Projection in the XY plane and (b) In the XZ plane.

can see that the magnitude of the highest values of density are considerably larger than those from the XY projection, with also a tight spread in the Z direction.

5.1.2 Particle densities and momentum distribution

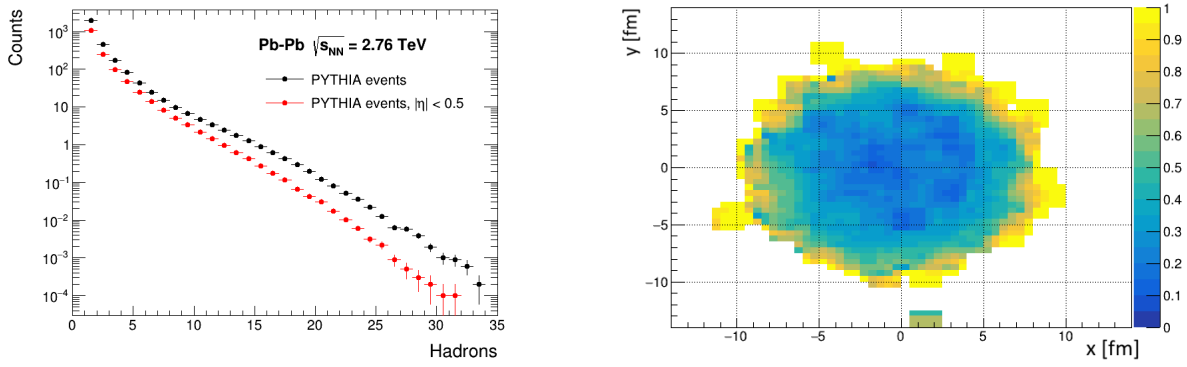

(a) (b)

Figure 5.6: (a) Distribution of particles with respect to the density of the cell where they are located, with the two curves comparing particles generated with (in red) and without (in black) an acceptance window in $|\eta|$. (b) Ratio of the sum of the absolute values of the momenta and the absolute value of the vector sum of momenta at $\eta_s = 0$. The grid resolution for this result is 0.5 fm.

Another way of understanding the modeled distribution is to calculate the densities of hadrons in each cell and their momentum configuration. The results of this first study is given in Fig. 5.6 (a), showing the number of cells with a certain number of particles, in arbitrary units, where most of those having no more than 10 hadrons, which results in the initial conditions with grids of lower densities of particles.

For the momentum configuration, however, the procedure was to define the ratio between the

modulus of the sum of momenta components and the sum of those moduli, with results from this calculation shown in Fig. 5.6 (b). Note that, as the ratio can range continuously from 0 to 1, some physical aspects of the distribution can also be observed: if equal to 1, this indicates the local existence of jets of particles, that is, there must be particles in the respective regions that are propagating in the same direction after the collision. Also, the chosen grid position indicates that, for $|\eta| < 0.8$, the momenta distribution of the center is such that there is a greater misalignment of hadrons, which is an expected result.

This study can also help develop an extension of the proposed model of initial conditions by including the momenta of the original particles in the $T^{\mu\nu}$, resulting then in a complete physical description of the initial stages through PYTHIA's modelling.

5.1.3 Initializing hydrodynamics

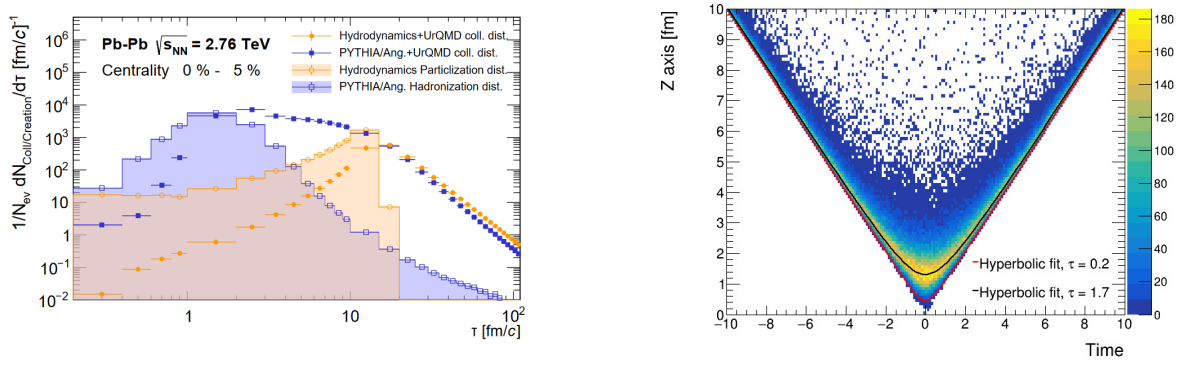

(a) (b)

Figure 5.7: (a) Results comparing the ratio of particle creation and collision distribution. (b) Light cone-like distribution of particles, where the hyperbolic fits are given by Eq. 5.1. Notice that the range $0 < \tau < 1.7$ fm/c includes the majority of the produced hadrons.

After the initial distribution is accounted for, the initialization parameters of hydrodynamics must be estimated, as done through Sec. 3.2. The initial time, however, has a connection to the hadronization rate of PYTHIA, as shown in Fig. 5.7 (a). As such, determining the best stage to start the hydrodynamic simulation was done through the space-time distribution of observed particles in Fig. 5.7 (b), which plots the number of particles with a given Z (η_s) position at time t. The correlation with the initial time of hydrodynamics is done knowing that this approach applies the Milne coordinates

$$\tau = \sqrt{t^2 - z^2}, \quad \eta_s = \frac{1}{2} ln \left(\frac{t+z}{t-z} \right), \tag{5.1}$$

to the evolution of the particlization surface, allowing for a simple approximation for τ. From this equation, the hyperbola shown in this figure were drawn, using first $\tau = 0.2$ fm/c, the standard initialization time for a hydrodynamic simulation using TRENTo as the initial condition generator, and later $\tau = 1.7$ fm/c, as this value encompasses most of PYTHIA's hadrons, as both figures on Fig. 5.7 indicates.

5.2 Final state observables

5.2.1 Multiplicity and momentum distribution

As mentioned in Sec. 4.1, the simulated events can be characterized using the number of particles as functions of transverse momenta, collision's centrality and angular distribution. The multiplicities of charged particles, N_{ch}, are one of the initial consistency metrics for the given outputs of any simulation, when compared to particle detector's results. The next few figures will present those results for simulated particles given by 2D and 3D approaches for initial conditions in a hydrodynamic chain. Also, as discussed in 3.2.1, the computational costs of running 3D hydrodynamics is considerably larger than in the 2D approach, and for that reason the data sample of the former is smaller than the latter. This may induce higher fluctuations and uncertainties in the following three-dimensional results.

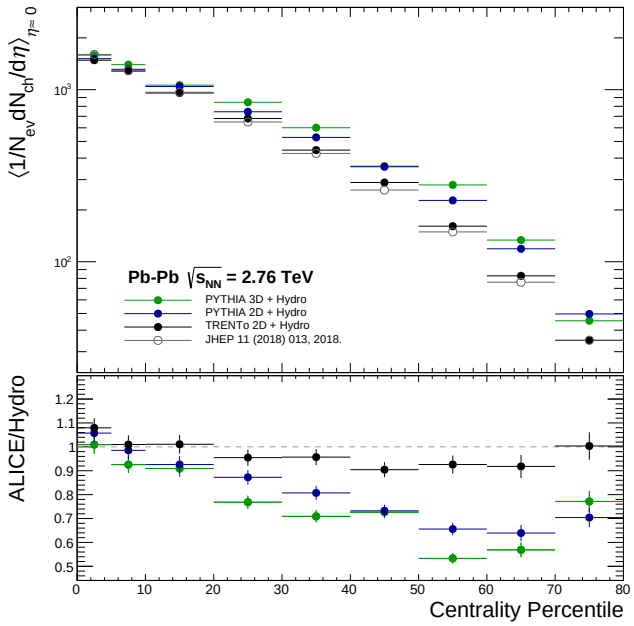

Figure 5.8: Charged particles for two and three dimensional simulations, with data from [59].

Fig. 5.8 shows the total number of charged particles, integrated in $0.2 < p_T < 5.0$ GeV/c, for

different classes of centrality, where each approach used its unique value of scale factor s in the initial conditions. That is, the initial distribution is multiplied by a given factor that directly affects the number of resulting particles, with the first centrality class generally being used as reference when calculating those normalization constants. For this figure, $s_{2D,\,P} = 0.357$ for PYTHIA 2D, $s_{2D,\,T} = 901.625$ for TRENTo 2D and $s_{3D} = 2.6$ for PYTHIA 3D. This is done to ensure that the output is consistent with the expected experimental results.

Notice that the results for PYTHIA presented in Fig. 5.8 shows an increasing divergence from simulation results on higher values of centrality, with two-dimensional simulations being slightly closer to data. Also, given that hydrodynamics is only a good approximation for non-peripheral events, as the volume of the simulated fluid in this case is enough for thermalization to occur and to the QGP to have an effect on the fluid's behavior, a certain level of divergence in data for those high-centrality events is expected. This will also be true for other observables, such as anisotropic flow in Sec. 5.2.2.

However, TRENTo's output for charged particles provides a more accurate description of experimental results. As a way to verify the extent of the description of this model, the distribution of momenta of all approaches must also be analysed. The resulting transverse momenta spectra of particles is shown in Figs. 5.9, with each individual spectra plotted for chosen centrality ranges, and 5.10, considering the mean over all centrality intervals.

In Figs. 5.9, while the particles generated with two and three-dimensional initial conditions have around the same magnitude for this given range of transverse momenta, with Figs. 5.9 (a) and (c) having few differences, the decrease in the number of particles for increasing p_T is faster for Fig. 5.9 (b). This indicates a smaller count of particles with high momenta for all centrality classes in the three-dimensional case, which translates in 3D simulations producing particles with smaller average momentum than their 2D counterpart. The reason for such characteristic of three-dimensional simulations is related to the substructure of the initial densities: differently from the smoother, two-dimensional initial conditions, which are given by integrating the energies and momentum of the η_s coordinate over the xy plane, the properties of those particles are kept in three-dimensional initial conditions, possibly producing a destructive interference at increasing momenta. Those hotspots of energy and momentum interact throughout the evolution of the initial density, where a smaller p_T will be produced as the momenta components are not summed in a projection of the xy plane. This same conclusion is given by the mean over centrality classes shown in Fig. 5.10. Although there are more particles with $p_T < 1.5$ GeV/c being predicted in the 3D approach than in the actual data in

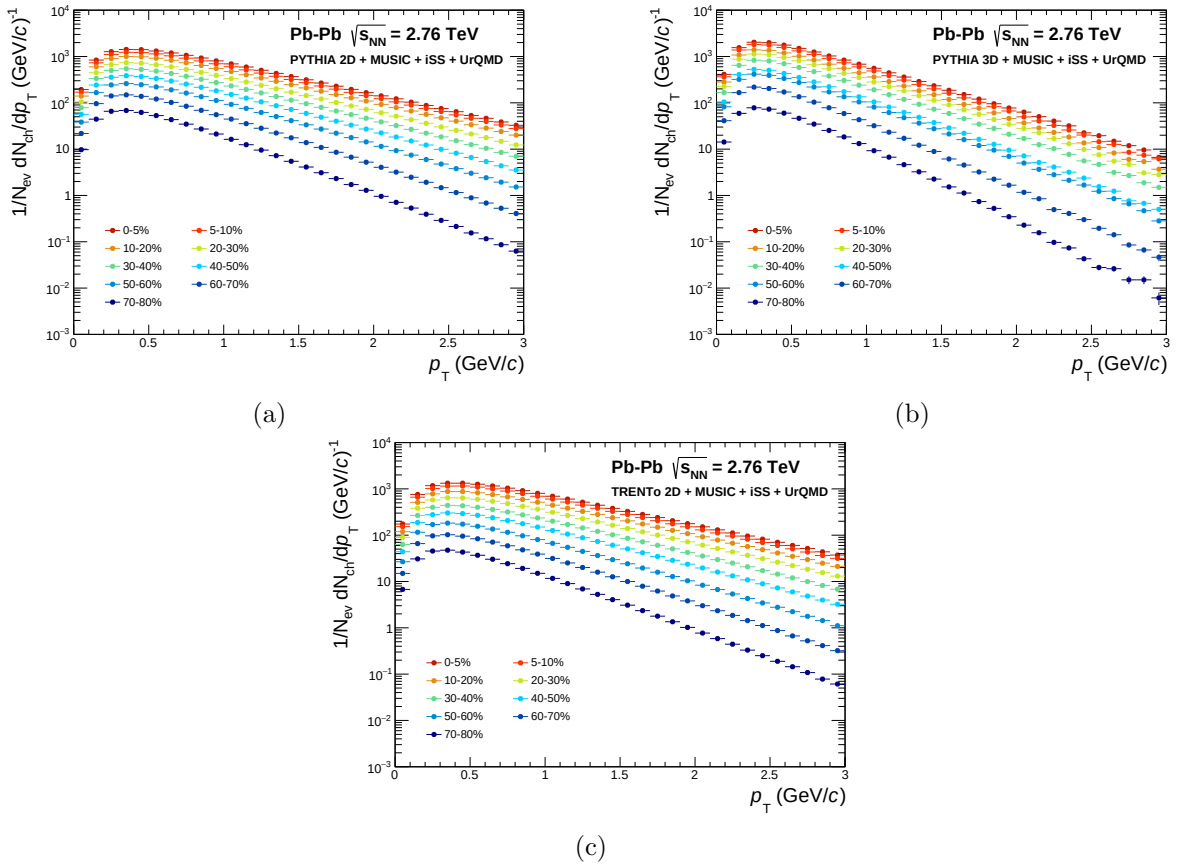

Figure 5.9: Transverse momenta spectra for hydrodynamic simulations for nine centrality classes using (a) two-dimensional and (b) three-dimensional PYTHIA initial conditions, and (c) TRENTo initial conditions.

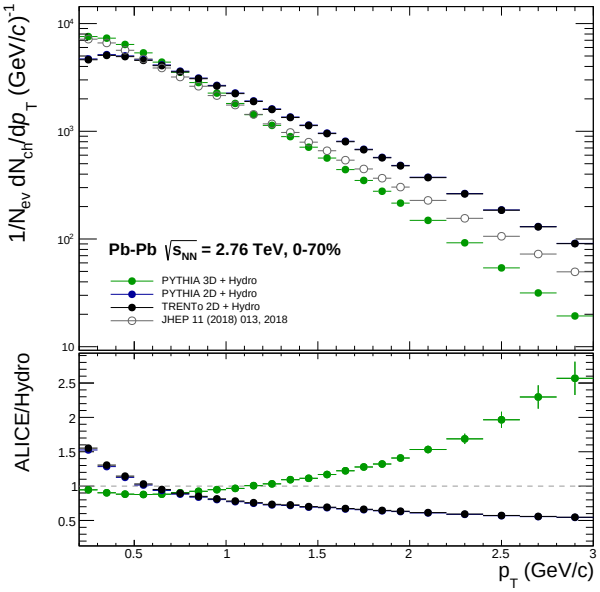

Figure 5.10: Comparison of PYTHIA and TRENTo results for p_T distribution integrated from 0 to 70% in centrality. Experimental data from [58].

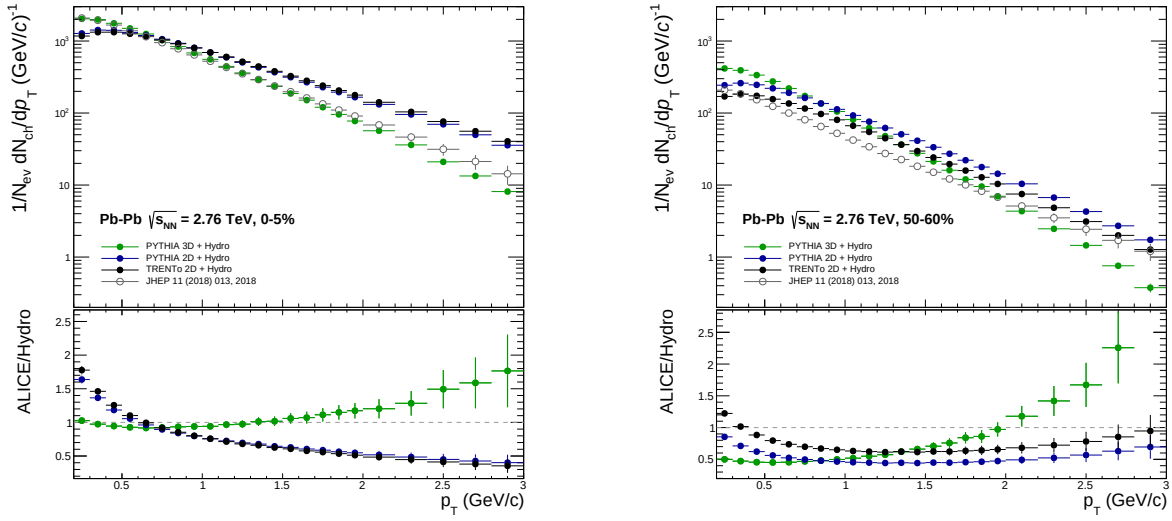

(a) (b)

Figure 5.11: Selected transverse momenta spectra and comparison to experimental data [58] for (a) central events $(0-5\%)$ and (b) peripheral events $(50-60\%)$.

this figure, the overall results pattern is closer to the measurements by the ALICE collaboration than the ones given by the 2D simulations, which have an almost identical output in momenta.

Upon inspecting the outputs of central events, this result becomes even clearer through Fig. 5.11, where two different centrality classes were compared to data: not only the spectra from central three-dimensional events follows the behavior of experimental results, but it is accurate within experimental uncertainty up to $p_T \approx 1.7$ GeV/c and presenting lower counts of particles while staying within 10% of data for the highest value of transverse momenta studied.

However, for peripheral events as shown in Fig. 5.11 (b), neither approaches describe experimental data, which corroborates the limitations of hydrodynamics as previously discussed. Also, as the spectra from 2D PYTHIA and TRENTo for this figure differs only in magnitude and not in behavior, the differences observed in Fig. 5.8 point to these approaches to initial conditions producing particles with diverse η distributions.

An important remark for the distribution of momenta observed for TRENTo's particles, as the above-mentioned figures feature a similar spectra for this model and 2D PYTHIA, is that the original tuning of the parameters used by the Duke collaboration, and also implemented in this project, does not include the transverse momenta distribution of particles.

5.2.2 Anisotropic flow results

Before presenting the results of this section, it is important to make some remarks on the centrality class and p_T interval chosen in the following figures. As discussed in [26], where the method of acquiring the experimental data of choice for this analysis is also discussed, the values for elliptic flow integrated in transverse momentum steadily increase from central to semi-peripheral collisions, reaching a maximum value for two-particle correlations at $40-50\%$ and, for four-particle correlations, at $50-60\%$ in centrality. Being the highest output of flow for heavy-ion collisions, the experimental results are also more readily available for the $s_{\mathrm{NN}} = 2.76$ TeV considered in this study. Notice that [26] also employs the cumulant method throughout their v_2 calculations.

However, the choice of centrality took into account the distribution of flow calculated for each approach and presented in Figs 5.12 as a parameter: while the two-dimensional simulations using PYTHIA follows the expected maximum for two-particle correlations discussed before and the pattern of data on Fig. 5.12 (a), the maximum for TRENTo's approach and the three-dimensional PYTHIA simulations, respectively, was shown to be at $40-50\%$ and $30-40\%$. Knowing that those are in the semi-peripheral range, the highest value of 3D PYTHIA was then used as a reference for latter discussions.

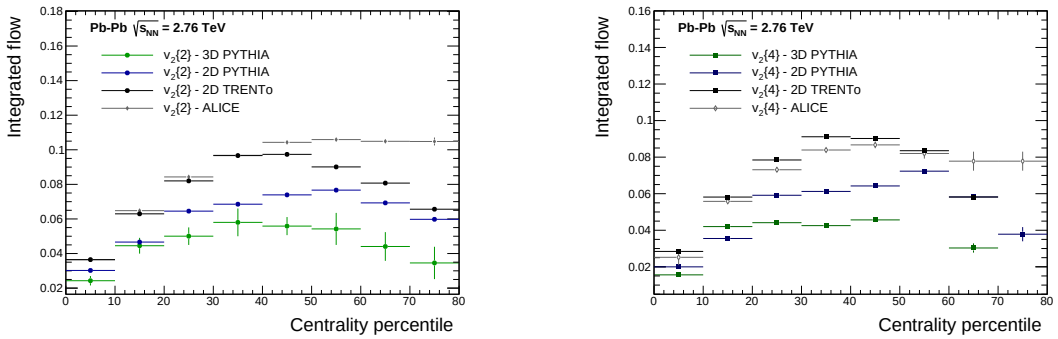

(a) (b)

Figure 5.12: Elliptic flow distribution ranging in centrality and integrated using $0.2 < p_T < 5.0$ GeV/c, where (a) includes two-particle correlation and (b) four-particle correlation results, with the latter excluding negative values observed in the centrality range of $50-70\%$. Experimental data from [26].

As for the transverse momenta range chosen, the intervals $0.2 < p_T < 3.0$ GeV/c and $0.2 < p_T < 3.2$ GeV/c were selected to display the differential flow results, as values greater than 3.2 GeV/c produce significantly more fluctuations and have an increased margin of uncertainty, although Fig.

5.12 maintains the experimental p_T range of $0.2 < p_T < 5.0$ GeV/c in its calculation.

Comparing each approach and their resulting anisotropy in centrality classes, it can be seen that although the behavior of simulated particles for the TRENTo approach is closely related to data up to centrality $30 - 40\%$, all approaches shows an increase in flow coefficients, which points to significant contributions from hydrodynamics and QCD predictions for the total observed anisotropy. It can also be said that the TRENTo + hydrodynamics model expects similar contributions from local and global phenomena, on central and semi-central events, as observed in data, given that those are more prominent for two-particle correlations. Also, hydrodynamics does not to produce enough anisotropy to describe the stability in $v_2\{2\}$ and slight decrease in $v_2\{4\}$ after the maximum value is reached in experimental data, which can be a result of the previous discussions of Sec. 5.2.1 regarding the validity of hydrodynamics for increasing centrality.

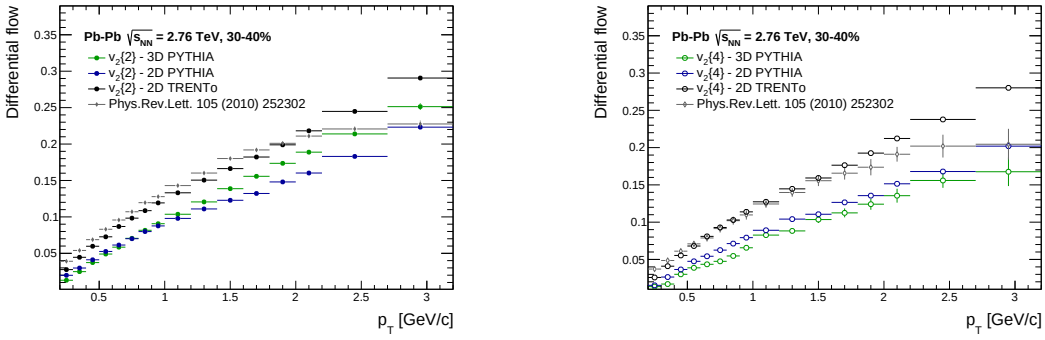

(a) (b)

Figure 5.13: Differential anisotropic flow outputs for the three hydrodynamic approaches, where (a) uses two-particle correlation for the associated calculations and (b) four-particle correlation. Experimental results from [26].

It is also possible to study the distribution of anisotropic flow using transverse momentum, characterizing the collective expansion of the fluid and the resulting modulation of the angle for the resulting particles with respect to their momenta. For two-particle correlation results given in Fig. 5.13 (a), the behavior observed for simulated TRENTo particles follows the same pattern presented by the data, with differences between each approach being given in different p_T ranges: PYTHIA + hydro simulations produce similar outputs for anisotropy for low momenta, with a fast increase in counts for the three-dimensional method after $p_T > 1.5$ GeV/c, nearing TRENTo's and experimental data with uncertainty bars considered at $p_T = 2.0$ GeV/c and beyond. This implies that, while the expected momenta distribution at low p_T for 3D is close to data, as shown in Fig. 5.10, the resulting anisotropy of such particles is still low, which can be a result of using hadrons produced at latter stages by

PYTHIA: the larger the momenta of such particles, the greater their distance from the center of the distribution will be, which can have an negative impact on the latter observed anisotropy. Including the contribution of the momenta in the initial condition and studying initial conditions with an earlier production of hadrons, however, could be a possible solution to the issue.

Four-particle correlation results, where less contributions from local phenomena are expected, also follows the behavior observed on the experimental distribution. TRENTo's approach predicts higher than data values for $p_T > 1.7$ GeV/c, meaning that the parametric initial conditions given by this method will expect higher values of anisotropy given by global effects. On the other hand, both PYTHIA approaches have lower-than-data values in the chosen p_T range, predicting a smaller influence of global effects on resulting particles.

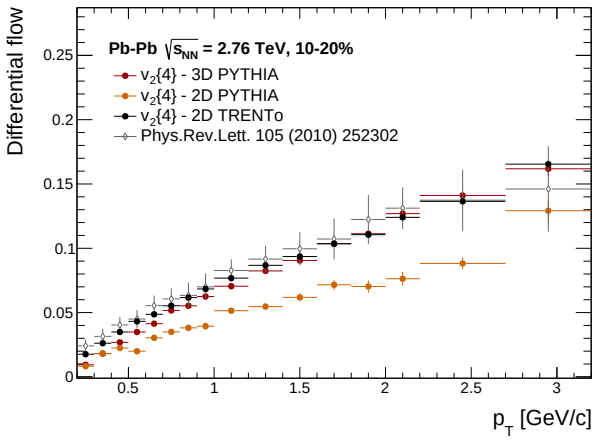

Figure 5.14: Elliptic flow with four-particle correlations for central events. Experimental data from [26].

Another comparison for elliptic flow results can be done using the anisotropy calculated for central events. Notice that, in Fig. 5.14, around $p_T > 0.8$ GeV/c all the flow coefficients for 3D simulations are comparable to data, considering their associated uncertainty, with results being similar to the TRENTo approach. Considering the greater accuracy of three-dimensional approach discussed in Sec. 5.2.1 on central events, the results of Fig. 5.14 also point to consider a 3D model to be a more appropriate way to describe anisotropic flow.

It is also important to study the behavior of higher harmonics, that is, v_n with $n > 2$. Here, triangular (v_3) and quadrangular (v_4) flow are presented in Figs. 5.15 for the centrality class of $30 - 40\%$, used previously on Figs. 5.13. Notice that, being higher order contributions, a higher degree of uncertainty and fluctuations are expected to be present in data.

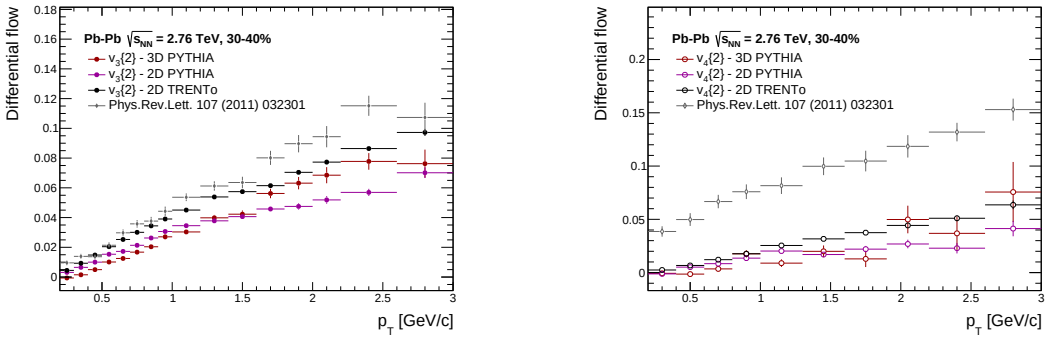

(a) (b)

Figure 5.15: Higher order anisotropy results for two and three-dimensional simulations. (a) triangular and (b) quadrangular flow, with experimental results from [64].

When compared, the approaches for hydrodynamics shows very distinct behaviors between themselves. While 2D TRENTo display results that are within uncertainty with data for $v_3\{2\}$ in low p_T ranges, 3D PYTHIA has a similar distribution to the former after $p_T = 1.5$ GeV. For Fig. 5.15 (b), it can be seen that none of the proposed methodologies describes data, that is, hydrodynamics does not produce large enough higher order anisotropy coefficients at v_4.

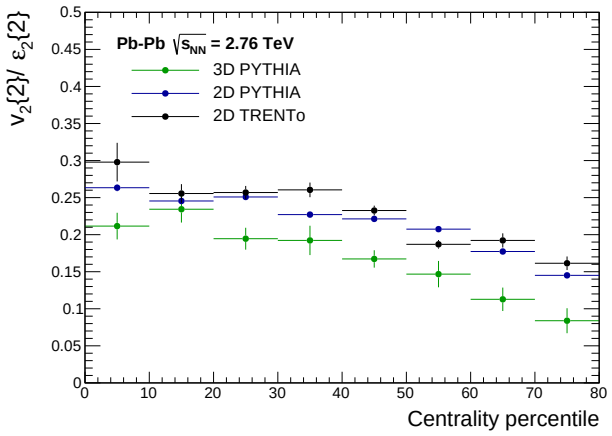

Figure 5.16: Ratio of elliptic flow to the eccentricity of a Pb+Pb collision for all approaches considered.

As for the impact of the geometry of the early stages of collision into the observed anisotropy of final particles that was discussed in Sec. 4.2.1. Fig. 5.16 shows the ratio of elliptic flow using two-particle correlations, $v_2\{2\}$, to the respective geometry of the original event calculated in first order, given by its eccentricity coefficient. This value can be interpreted as a response coefficient of hydrodynamics-based evolution, i.e. $v_2 = \alpha\varepsilon_2$. In this figure, it can be seen that the resulting ratios for each approach presents an almost constant behavior for central events, with a steady decrease in

modulus for increasing centralities. This latter pattern can be understood considering the reduction of calculated flow for peripheral events, as shown in Fig. 5.12 and discussed previously. For central events, the increase in modulus for elliptic flow is proportional to the result observed in Fig. 5.4 (a), pointing to the original substructure of a head-on event having greater influence over the observed collective behavior of final particles.

Also, the original distribution causes less impact on three-dimensional PYTHIA simulations, which indicate that this initial condition generates an anisotropy profile that is less sensitive to local phenomena than the other approaches on higher centralities, which was also observed on Fig. 5.13 (b). Additionally, all ratios being less than one means that the hydrodynamic response to the initial density results in a final distribution that is less elliptic when compared to the stages immediately after the collision. This response can be different when not considering the attenuation effects caused by viscosity: an ideal hydrodynamic simulation could potentially result in a more elliptical final shape, and therefore a somewhat larger response coefficient $\alpha = v_2/\varepsilon_2$.

Conclusions and outlook

This project developed a new methodology to generate initial distributions for hydrodynamics simulations using the resulting hadrons generated by PYTHIA, which is inspired on QCD and includes multiple physical processes not considered by other alternatives used to simulate heavy-ion collisions. A systematic study of such initial conditions from PbPb collisions was performed, with those being either longitudinally invariant or fully three-dimensional, with the resulting output being used in a hydrodynamics simulation chain. The results from our simulations were then explored in detail.

These initial conditions were generated by assigning a gaussian distribution to each hadron, generating the density profile in two or three dimensions necessary to initialize the hydrodynamic evolution. These profiles were then characterized using their geometric properties: Sec. 5.1 shows that PYTHIA initial conditions are composed of more hotspots, that is, structures with higher density than the average of the distribution, than the alternative given by TRENTo and used as baseline. Moreover, those former profiles were also shown to be smoother for central events, but forming lumpier structures when considering centralities larger than 50%.

The next stage was to fully develop a hydrodynamic evolution by coupling those initial conditions to a hydrodynamics-based simulation chain. The study presented in Sec. 5.2 made extensive comparisons between using two and three-dimensional initial conditions and experimental data from the ALICE collaboration. When comparing each approach for the initial profile, it was shown that the gradients generated by including a third dimension have a different outcome from the 2D densities, given that the latter projects the spatial rapidity component of hadrons into a plane. Moreover, the results from 3D PYTHIA provide an accurate description of the transverse momentum spectra of particles, specially when analysing central events. The addition of the third dimension, and the fact that it has significant effects on the evolution of the initial density discussed in 5.2, indicates that this component should not be neglected and might be essential to an accurate description of a heavy-ion system.

Another observable explored in this work was the anisotropic flow, which characterizes collective behavior of final particles through a modulation of their azimuthal emission angle. All results have

demonstrated the same behavior of differential elliptic flow, the second order anisotropy coefficient, on central and semi-central collisions, given the limits of the hydrodynamic approach discussed in 5.2.1. Additionally, PYTHIA's 3D approach displayed greater accuracy for increasingly central collisions for v_2, while also predicting lower anisotropy coefficients than TRENTo and experimental data, with such contrast being more relevant for four-particle correlations, where global effects are more prevalent and thus influence the final distribution more strongly. Moreover, the ratio of elliptic flow to the eccentricity of the initial density was also calculated, showing an approximately constant hydrodynamic response in central events and a decrease of the influence from the initial stages for peripheral events.

As mentioned in Sec. 2.4, the generated initial conditions presented in this study only include contributions from the spatial positions of hadrons produced in PYTHIA to formulate the density distribution. The physics of such approach has the potential of improving significantly if the momenta of those hadrons are also included as components of this initial profile. The hadron densities and momentum distribution of the new initial conditions have already been studied in Sec. 5.1, with those results being essential to initiate this extension. Along with the use of momenta, another possible approach to improve this model would be to develop a modification for the PYTHIA code that allows the use of partons directly, excluding the necessity of using its hadrons to generate an initial density. Furthermore, given that the original hydrodynamic parameters, such as the transport coefficients, were initially tuned for two-dimensional initial densities, reevaluating those variables for a three-dimensional simulation would be beneficial not only for this project, but also to other initial stage methods, as these calculations including three-dimensional parameters have not yet been done.

Bibliography

1. Glashow, S. L. Partial-symmetries of weak interactions. *Nuclear Physics* **22,** 579–588. ISSN: 0029-5582 (1961).
2. Weinberg, S. A Model of Leptons. *Phys. Rev. Lett.* **19,** 1264–1266 (21 Nov. 1967).
3. Salam, A. Elementary Particle Physics: Relativistic Groups and Analyticity. *In: N. Svartholm, Ed., Eighth Nobel Symposium* (1968).
4. Biever, C. *It's a boson! But we need to know if it's the Higgs* 2012. https://www.newscientist.com/article/dn22029-its-a-boson-but-we-need-to-know-if-its-the-higgs/#ixzz7EN0vy2RM.
5. O'Luanaigh, C (CERN). *New results indicate that new particle is a Higgs boson* 2013. https://home.web.cern.ch/news/news/physics/new-results-indicate-new-particle-higgs-boson.
6. Naik, G. *New Data Boosts Case for Higgs Boson Find* 2013. https://www.wsj.com/articles/SB10001424127887324077704578359850108689618.
7. The Pierre Auger Collaboration. *The Pierre Auger Observatory Upgrade - Preliminary Design Report* 2016. arXiv: 1604.03637 [astro-ph.IM].
8. Pontecorvo, B. Neutrino Experiments and the Problem of Conservation of Leptonic Charge. *Soviet Physics— JETP* **26,** 984 (1968).
9. Deur, A., Brodsky, S. J. & de Téramond, G. F. The QCD running coupling. *Progress in Particle and Nuclear Physics* **90,** 1–74. ISSN: 0146-6410 (Sept. 2016).
10. Thomson, M. *Modern Particle Physics* ISBN: 978-1-107-03426-6 (Cambridge University Press, 2013).
11. Wong, C. *Introduction to high-energy heavy-ion collisions* (World scientific, Singapore, 1994).

12. Adams, J. *et al.* Experimental and theoretical challenges in the search for the quark gluon plasma: The STAR Collaboration's critical assessment of the evidence from RHIC collisions. *Nucl. Phys.* **A757,** 102–183. arXiv: nucl-ex/0501009 [nucl-ex] (2005).

13. Chinellato, D. D. *Estudo de estranheza em colisões próton-próton no LHC* PhD thesis (Universidade Estadual de Campinas, Instituto de Física Gleb Wataghin, Campinas, SP, 2012).

14. Bzdak, A. *et al.* Mapping the phases of quantum chromodynamics with beam energy scan. *Physics Reports* **853,** 1–87. ISSN: 0370-1573 (Apr. 2020).

15. Vogt, R. *Ultrarelativistic Heavy-Ion Collisions* 221–278. ISBN: 978-0-444-52196-5 (Elsevier Science B.V., Amsterdam, 2007).

16. Back, B. *et al.* The PHOBOS perspective on discoveries at RHIC. *Nuclear Physics A* **757,** 28–101. ISSN: 0375-9474 (Aug. 2005).

17. Nagle, J. L. & Zajc, W. A. Small System Collectivity in Relativistic Hadronic and Nuclear Collisions. *Annual Review of Nuclear and Particle Science* **68,** 211–235. ISSN: 1545-4134 (Oct. 2018).

18. Van Hove, L. C. P. Multiplicity dependence of p_t spectrum as a possible signal for a phase transition in hadronic collisions. *Phys. Lett. B* **118,** 138–140 (July 1982).

19. Rafelski, J. & Müller, B. Strangeness Production in the Quark-Gluon Plasma. *Phys. Rev. Lett.* **48,** 1066–1069 (Apr. 1982).

20. The CMS collaboration. Measurement of jet fragmentation into charged particles in pp and PbPb collisions at $\sqrt{s_{NN}}$=2.76 TeV. *J. High Energ. Phys* **87** (2012).

21. Frixione, S. *et al.* Heavy-Quark Production. *Adv.Ser.Direct.High Energy Phys.* **15,** 609–706 (1998).

22. Borcsik, F. S. *Estudo da influência das condições iniciais em colisões nucleares ultrarrelativísticas* MA thesis (Universidade Estadual de Campinas, Instituto de Física Gleb Wataghin, Campinas, SP, 2018).

23. Perkins, D. H. *Introduction to high energy physics* (Cambridge university Press, 2000).

24. Christensen, C. H. *Fluctuations in Au+Au collisions at 200 GeV.* MA thesis (Niels Bohr Institute, University of Copenhagen, 2003).

25. Abelev, B. *et al.* Centrality determination of Pb-Pb collisions at $\sqrt{s_{NN}} = 2.76$ TeV with ALICE. *Phys. Rev. C* **88,** 044909 (4 Oct. 2013).

26. Aamodt, K. *et al.* Elliptic Flow of Charged Particles in Pb-Pb Collisions at $\sqrt{s_{NN}} = 2.76$ TeV. *Phys. Rev. Lett.* **105,** 252302 (25 Dec. 2010).

27. Alver, B. & Roland, G. Collision-geometry fluctuations and triangular flow in heavy-ion collisions. *Phys. Rev. C* **81,** 054905 (5 May 2010).

28. Qin, G.-Y., Petersen, H., Bass, S. A. & Müller, B. Translation of collision geometry fluctuations into momentum anisotropies in relativistic heavy-ion collisions. *Physical Review C* **82.** ISSN: 1089-490X (Dec. 2010).

29. Eyyubova, G. K., Korotkikh, V. L., Snigirev, A. M. & Zabrodin, E. E. Eccentricities, fluctuations and A-dependence of elliptic and triangular flows in heavy-ion collisions. *Journal of Physics G: Nuclear and Particle Physics* **48,** 095101. ISSN: 1361-6471 (Aug. 2021).

30. Noronha-Hostler, J., Yan, L., Gardim, F. G. & Ollitrault, J.-Y. Linear and cubic response to the initial eccentricity in heavy-ion collisions. *Physical Review C* **93.** ISSN: 2469-9993 (Jan. 2016).

31. McDonald, S., Jeon, S., Gale, C. IP-Glasma Phenomenology Beyond 2D. *Nuclear Physics A* **982,** 239–242. ISSN: 0375-9474 (Feb. 2019).

32. Drescher, H. J., Liu, F. M., Ostapchenko, S., Pierog, T. & Werner, K. Initial condition for quark-gluon plasma evolution. *Phys. Rev. C* **65,** 054902 (5 Apr. 2002).

33. Bernhard, J. E., Moreland, J. S., Bass, S. A. Alternative ansatz to wounded nucleon and binary collision scaling in high-energy nuclear collisions. *Phys. Rev. C* **92,** 011901 (1 July 2015).

34. Bernhard, J. E., Moreland, J. S., Bass, S. A. *Reduced Thickness Event-by-event Nuclear Topology (TRENTo) official website* http://qcd.phy.duke.edu/trento/.

35. Sjöstrand, T., Mrenna, S. & Skands, P. PYTHIA 6.4 physics and manual. *Journal of High Energy Physics* **2006,** 026–026. ISSN: 1029-8479 (May 2006).

36. Sjöstrand, T., Mrenna, S. & Skands, P. *PYTHIA 8.235 Online Manual* https://pythia.org/manuals/pythia8235/Welcome.html.

37. Prestel, S. *The Lund Hadronization Mode* https://indico.cern.ch/event/727283/contributions/3102176/.

38. Sjöstrand, T. *et al.* An introduction to PYTHIA 8.2. *Computer Physics Communications* **191,** 159–177. ISSN: 0010-4655 (June 2015).

39. Sjöstrand, T. *Torbjörn Sjöstrand - Talks (homepage)* http://home.thep.lu.se/~torbjorn/welcomeaux/talks.html.

40. Bierlich, C., Gustafson, G. & Lönnblad, L. Diffractive and non-diffractive wounded nucleons and final states in pA collisions. *Journal of High Energy Physics* **2016.** ISSN: 1029-8479 (Oct. 2016).

41. Pi, H. An event generator for interactions between hadrons and nuclei — FRITIOF version 7.0. *Computer Physics Communications* **71,** 173–192 (Aug. 1992).

42. Silva, A. V. d. *Simulating heavy-ion collisions using a hybrid model based on QCD and hadronic rescattering* Doutorado em Física (Universidade Estadual de Campinas, Instituto de Física Gleb Wataghin, Campinas, SP, 2020).

43. Fu, B., Xu, K., Huang, X.-G. & Song, H. Hydrodynamic study of hyperon spin polarization in relativistic heavy ion collisions. *Physical Review C* **103.** ISSN: 2469-9993 (Feb. 2021).

44. The MADAI collaboration. *Heavy-ion collisions* http://madai.phy.duke.edu/indexaae2.html?page_id=503.

45. Molnár, E., Niemi, H., Denicol, G. S. & Rischke, D. H. Relative importance of second-order terms in relativistic dissipative fluid dynamics. *Phys. Rev.* **D89,** 074010. arXiv: 1308.0785 [nucl-th] (2014).

46. Denicol, G. S., Niemi, H., Molnar, E. & Rischke, D. H. Derivation of transient relativistic fluid dynamics from the Boltzmann equation. *Phys. Rev.* **D85.** [Erratum: Phys. Rev.D91,no.3,039902(2015)], 114047. arXiv: 1202.4551 [nucl-th] (2012).

47. Denicol, G. S., Jeon, S. & Gale, C. Transport coefficients of bulk viscous pressure in the 14-moment approximation. *Phys. Rev. C* **90,** 024912 (2 Aug. 2014).

48. Paquet., J.-F. *Simulating heavy ion collisions with MUSIC* (2018). https://webhome.phy.duke.edu/~jp401/music_manual/.

49. Bernhard, J. E., Moreland, J. S., Bass, S. A. et. al. Applying Bayesian parameter estimation to relativistic heavy-ion collisions: Simultaneous characterization of the initial state and quark-gluon plasma medium. *Physical Review C* **94.** ISSN: 2469-9993 (Aug. 2016).

50. Bernhard, J. E., Moreland, J. S. *hic-eventgen: Stripped down version of the hic-eventgen code, used only to generate an EOS* https://github.com/j-f-paquet/eos_maker.

51. Shuryak, E. Strongly coupled quark-gluon plasma in heavy ion collisions. *Rev. Mod. Phys.* **89,** 035001 (3 July 2017).

52. Rose, J.-B., Torres-Rincon, J. M., Schäfer, A., Oliinychenko, D. R. & Petersen, H. Shear viscosity of a hadron gas and influence of resonance lifetimes on relaxation time. *Physical Review C* **97.** ISSN: 2469-9993 (May 2018).

53. Huovinen, P. & Petersen, H. Particlization in hybrid models. *The European Physical Journal A* **48.** ISSN: 1434-601X (Nov. 2012).

54. Cooper, F. & Frye, G. Single-particle distribution in the hydrodynamic and statistical thermodynamic models of multiparticle production. *Phys. Rev. D* **10,** 186–189 (1 July 1974).

55. Frankfurt Institute for Advanced Studies. *Ultrarelativistic Quantum Molecular Dynamics (UrQMD) official website* https://urqmd.org/.

56. Sorensen, P. in *Quark-gluon plasma 4* (eds Hwa, R. C. & Wang, X.-N.) 323–374 (World Scientific, 2010). arXiv: 0905.0174 [nucl-ex].

57. Poskanzer, A. M. & Voloshin, S. A. Methods for analyzing anisotropic flow in relativistic nuclear collisions. *Phys. Rev. C* **58,** 1671–1678 (3 Sept. 1998).

58. Acharya, S. *et al.* Transverse momentum spectra and nuclear modification factors of charged particles in pp, p-Pb and Pb-Pb collisions at the LHC. *Journal of High Energy Physics* **2018.** ISSN: 1029-8479 (Nov. 2018).

59. Aamodt, K. *et al.* Centrality Dependence of the Charged-Particle Multiplicity Density at Midrapidity in Pb-Pb Collisions at $\sqrt{s_{\mathrm{NN}}} = 2.76$ TeV. *Phys. Rev. Lett.* **106,** 032301 (3 Jan. 2011).

60. Ollitrault, J.-Y., Poskanzer, A. M. & Voloshin, S. A. Effect of flow fluctuations and nonflow on elliptic flow methods. *Phys. Rev. C* **80,** 014904 (1 July 2009).

61. Borghini, N., Dinh, P. M. & Ollitrault, J.-Y. Flow analysis from multiparticle azimuthal correlations. *Phys. Rev. C* **64,** 054901 (5 Sept. 2001).

62. Luzum, M. Flow fluctuations and long-range correlations: elliptic flow and beyond. *Journal of Physics G: Nuclear and Particle Physics* **38,** 124026. ISSN: 1361-6471 (Nov. 2011).

63. Teaney, D. & Yan, L. Triangularity and dipole asymmetry in relativistic heavy ion collisions. *Phys. Rev. C* **83,** 064904 (6 June 2011).

64. Aamodt, K. *et al.* Higher harmonic anisotropic flow measurements of charged particles in Pb-Pb collisions at $\sqrt{s_{NN}}$=2.76 TeV. *Phys. Rev. Lett.* **107,** 032301. arXiv: 1105.3865 [nucl-ex] (2011).